DEVELOPMENT OF DUAL-MODALITY OPTICAL IMAGING SYSTEMS CONSISTING OF OPTICAL COHERENCE TOMOGRAPHY AND FLUORESCENCE LIFETIME IMAGING MICROSCOPY

A Dissertation

by

SEBINA SHRESTHA

Submitted to the Office of Graduate and Professional Studies of
Texas A&M University
in partial fulfillment of the requirements for the degree of

DOCTOR OF PHILOSOPHY

Chair of Committee,	Brian E. Applegate
Committee Members,	Javier A. Jo
	Kristen C. Maitland
	Ohannes Eknoyan
Head of Department,	Gerard Coté

August 2015

Major Subject: Biomedical Engineering

ABSTRACT

Both morphological and biochemical changes occur in a diseased tissue. As a result, tissue optical response changes with the progression of disease. A single optical imaging modality can assess either morphological or biochemical changes. In order to investigate the development of a disease in detail, both of these characteristics need to be probed simultaneously. Therefore, researchers have been interested in combining different imaging modalities that can provide complementary, morphological and biochemical images. This dissertation focuses on the development of dual-modality systems that incorporate Optical coherence Tomography (OCT) and Fluorescence Lifetime Imaging Microscopy (FLIM) for simultaneous characterization of tissue morphology and its biochemistry.

In the first phase of the research, we combined spectral-domain OCT with FLIM that is designed for endogenous emission acquisition. The operating wavelength for OCT and FLIM were 830nm and 355nm, respectively. The maximum field of view (FOV) was 4mmx4mm. The combined system was used to image hamster cheek pouch model for oral cancer *in vivo* and postmortem human coronary arteries with atherosclerotic plaques *ex vivo*. Their morphological and endogenous emission images correlation was studied. The evaluation was equivalent to their histopathological analysis.

In the second phase of this research, we built a bench-top prototype that comprised of swept source OCT (SSOCT) and a FLIM system with the capability to

characterize endogenous and exogenous emissions simultaneously. The swept laser had a sweep rate of 50 kHz and the center wavelength was at 1310nm. FLIM utilized lasers with wavelengths 355nm and 532nm to excite endogenous and exogenous fluorophores, respectively. The maximum FOV was 16mmx16mm. With this system, OCT-FLIM images of a Watanabe rabbit aorta, which was non-specifically tagged with Alexa Fluor 532, were acquired *ex-vivo*. The results appraised the ability of the system to simultaneously probe the sample's structure, its endogenous emission and the exogenous fluorescence of the dye tagged to it. We hypothesize that the OCT-FLIM imaging tool adds a potential to study the activities of important non-fluorescing molecules in an artery while relating the analysis to its morphology and biochemistry.

DEDICATION

To my parents.

ACKNOWLEDGEMENTS

I offer my sincere gratitude to my advisors Dr. Brian Applegate and Dr. Javier Jo for introducing me to this prodigious field of research, which has ended up becoming my fervor. I am grateful for their guidance and support during my journey at Texas A&M University (TAMU). I must say I learnt every aspect of optical imaging system design, development, testing and troubleshooting, while working closely with Dr. Applegate. Likewise, Dr. Jo helped me a lot in assimilating animal studies, sample preparation for imaging as well as histopathological processing, and the motivation to such research. I always admired their depth of knowledge in many sectors of science and engineering, and their teaching approach in lab.

I would like to thank Dr. Kristen Maitland for helping me understand the fundamentals of optics in her course – Biophotonics. Also, her method of well-organized research has inspired me.

I am thankful to Dr. Ohannes Eknoyan for teaching one of the most interesting classes, Optoelectronics, during my graduate studies. I would also like to thank him for his time and energy to serve on my committee.

I would also like to appreciate Dr. Jesung Park for his tremendous guidance on system synchronization and testing, writing codes for image acquisition and processing, and animal studies. Also, my special thanks goes to all other former and current team members of this OCT-FLIM project- Paritosh Pande, Dr. Xudong Xiao, Elsie Ponch, Xi Chen, Julia Buck, Michael Serafino and Jesus Rico Jimenez.

I would like to thank Dr. Irma Gimenez-Conti and Jimi Brandon from University of Texas M.D. Anderson Cancer center for providing guideline in animal studies. I owe a remarkable gratitude to Dr. Fred Clubb from the Department of Veterinary Pathobiology, TAMU and Dr. Jessie Adame from Autopsy and Pathology Services, Kingwood, TX for incessant provision of valuable samples of post mortem human coronary artery.

I would also like to acknowledge our collaborator at Texas Heart Institute (THI), Dr. Brian Walton for his suggestions and support. I appreciate him for motivating me with his vision for clinical application of an OCT-FLIM imaging system in patients during cardiac surgery. Similarly, thanks to Dr. Siqin Zhaorigetu for his help with aorta extraction from animals and protocol for tagging molecules in artery. Also, I would like to thank Rosalva Munoz for all the administrative support and her effort to make Houston my new home during the transition. Thanks to Dinah Leslie for helping me with all the shipments at THI.

I would also like to thank Dr. Patrick Kee and Sidney Sherwood from The University of Texas Health Science Center at Houston for providing aorta of Watanabe Rabbits. Also, Thanks to Dr. Jonathan Lu from THI for the suggestions on the procedure of tagging LOX-1.

I would like to extend my appreciation to Desmond Jacob, Janey Wan and Ryan Shelton for their warm welcome to the lab and for patiently providing inkling to solution to my research hurdles as a rookie. Also, I want to thank Chintan Trivedi, Aditi Dabir, Patrick Thomas, Shuna Cheng, Nilanthi Warnasooriya, Wihan Kim, Esteban Carbajal,

Jeremy Pearson, Scott Mattison and Sangmin Kim for their suggestions and support. Thanks to Barbara Slusher for placing numerous orders for this research.

I would like to take this opportunity to express my gratitude to my grandmother who through her sacrifice and contribution has brought the family where it stands today. Thanks to my Opa and Oma for their love and encouragement all my life. My deepest gratitude goes to my parents who have constantly loved and encouraged me, and have supported my career and lifestyle choices. Thanks to my uncles and aunts for being my role model in some way or the other. Last but not least, big thanks to my companions through thick and thin - my brother, closest cousins and my friends forever.

NOMENCLATURE

BSA	Bovine Serum Albumin
CNC	Calcified Necrotic Core
DOF	Depth of Focus
FAD	Flavin Adenine Dinucleotide
FDOCT	Frequency-domain Optical Coherence Tomography
FLIM	Fluorescence Lifetime Imaging Microscopy
FOV	Field of View
FWHM	Full Width at Half of Maximum
IVUS	Intravascular Ultrasound
LDL	Low-density Lipoprotein
MMF	Multi-mode fiber
MRI	Magnetic Resonance Imaging
NA	Numerical Aperture
NADH	Nicotinamide Adenine Dinucleotide
NIR	Near Infrared
OCT	Optical Coherence Tomography
oxLDL	Oxidized Low-density Lipoprotein
PBS	Phosphate Buffer Saline
PMT	Photo-Multiplier Tube
POPOP	1,4-bis(5-phenyloxazol-2-yl) benzene

SDOCT	Spectral-Domain Optical Coherence Tomography
SMF	Single-mode fiber
SNR	Signal-to-Noise Ratio
SSOCT	Swept Source Optical Coherence Tomography
TDOCT	Time-domain Optical Coherence Tomography
TFC	Thick Fibrotic Cap
TRFS	Time-resolved Fluorescence Spectroscopy
UV	Ultra-violet
VCAM-1	Vascular Cell Adhesion Molecule-1
WHHL	Watanabe Heritable Hyperlipidaemic
WHO	World Health Organization

TABLE OF CONTENTS

Page

Page

LIST OF FIGURES

Page

Page

1. INTRODUCTION*

1.1 Background

Research in biomedical engineering focuses on the application of available engineering principles and techniques to decrease disease morbidity and mortality. One of the sectors investigates the development of non-or minimally invasive optical imaging tools for timely and/or detailed diagnosis of the diseases. Currently, two diseases that require well-engineered diagnostic tools are oral cancer and atherosclerosis.

Oral cancer is associated with the development of malignant tissue in oral cavity and larynx. The Oral Cancer Foundation estimates that more than 45,750 new cases of oral cancer will be reported this year in the US [2]. The average 5 year survival rate of oral cancer at all stages is approximately 57% and this figure hasn't shown much improvement in the last decade [2]. This lies on the fact that the symptoms are evident only in a later stage, in most cases, when the cancer metastasizes to the lymph node of the neck, making the treatment difficult and expensive [3]. Late diagnosis of oral cancer can also be attributed to the conventional method of diagnosis used in clinics. It primarily involves visual inspection which is followed by biopsies at few suspicious regions. Since distinction between benign and malignant lesion is not visually clear at early stages, the chances of failing to detect a precancerous region is high. Moreover, the

---

* Parts of this section were taken from [1] J. Park, J. A. Jo, S. Shrestha, P. Pande, Q. Wan, and B. E. Applegate, "A dual-modality optical coherence tomography and fluorescence lifetime imaging microscopy system for simultaneous morphological and biochemical tissue characterization," *Biomed Opt Express*, vol. 1, pp. 186-200, 2010. Copyright 2015 The Optical Society.

procedure of biopsy is painful to the patient and taking biopsy at every suspicious region is impractical. As a result, regular examination of the oral cavity for premalignant tissue is often overlooked. However, based on the study conducted by The Oral Cancer Foundation, early detection of oral cancer is the key to the survivability of oral cancer. The foundation estimates that early detection of oral cancer can significantly improve the survival rate by as much as 80-90%. From this it is evident that the number of early detections can be greatly improved if an alternative to biopsy is available, which is easier and faster to carry out. This underscores the need of a tool which can non-invasively diagnose oral cancer at early stage.

Likewise, atherosclerosis is a process of hardening of an artery to form plaques on the lumen. It is a gradual process that begins as fatty streaks at childhood and may lead to occlusion at older ages. Ischemic heart diseases and stroke, which have been the top two causes of death in the world in the last decade according to World Health Organization (WHO), are caused by atherosclerosis [4]. Atherosclerosis may also be the reason for many other diseases, e.g. peripheral artery disease, chronic kidney disease, depending on its location. To mitigate risk from this condition, pharmaceutical methods to cease aggravation of atherosclerosis are being clinically used or are under research [5, 6]. Research also shows that the development of atherosclerosis is in stages accompanied by minute changes in the artery, meaning the therapeutic strategy depends on the condition of the hardening. Therefore, diagnostic tools that help in comprehensive visualization of the plaques are important to increase the efficacy of atherosclerosis treatment. Current clinically used technologies, such as angiography and intravascular

ultrasound, only help in identifying blockages in the lumen or plaques on the vascular bed. However, atherosclerosis is a complex process that requires more detailed assessment of the plaques in order to be able to classify them accurately for the most suitable treatment. Therefore, further investigation on the development of a diagnostic tool that screens the arteries in molecular level and that classifies atherosclerotic plaques with high sensitivity and specificity is essential.

In general, diagnostic tools assess the biomarkers of a disease. Therefore, identifying the biomarkers is essential before selecting/developing an intervention. The changes in tissue during the progression of oral cancer and atherosclerosis are discussed below at a basic level:

1. Oral epithelial tissue consists of layers of stratified squamous epithelium of several cell layers thickness, a basement membrane of a single cell layer thickness and a stromal region with collagen and blood vessel. Malignant cells originate at the basement membrane and proliferate upward to the epithelium. With further growth of these cells, they invade into the stroma by breaking the basement membrane. During this process, the structural modifications incident on the oral epithelium are, formation of keratin, epithelial thickening, loss or destruction of layered structure and irregular epithelial stratification [7-10]. Oral epithelial tissue also experiences degradation of stromal collagen as well as an elevation in metabolic rate elevation and cellular invasion. The

NADH-FAD* activity increases leading to an increase in the concentration of NADH and decrease in the concentration of FAD at abnormal state [11, 12].

2. A basic structure of an artery consists of layers of intima, media and adventitia. Intima contains endothelial cells of a cell layer thickness. Media is made of smooth muscle cells and elastic fibers containing elastin. Adventitia is composed of connective tissue consisting of collagen. Atherosclerosis involves the development of various forms of plaques in the intimal region, as summarized in Figure 1. It begins with the development of pathological intimal thickening filled with collagen. During this process, lipoproteins such as Low-Density Lipoprotein (LDL) may enter the intima, get oxidized, get accumulated, and as a result may lead to generation of lipid-rich foam cells[13]. In the subsequent stage, smooth muscle cells may form fibrous cap over the foam cells forcing the formation of necrotic core. Necrotic cores may be inflamed and/or calcified. Also, the thickness of the fibrous cap may differ**.

From this discussion on the changes of oral epithelium and arterial intima, we can recognize that they go through several morphological and biochemical changes during the progress of the disease. Therefore, these changes can be considered the biomarkers for their diagnosis.

---

* NADH- Nicotinamide Adenine Dinucleotide, FAD- Flavin adenine nucleotide

** The structure and the process of atherosclerosis are far more complex than described and beyond the scope of this study.

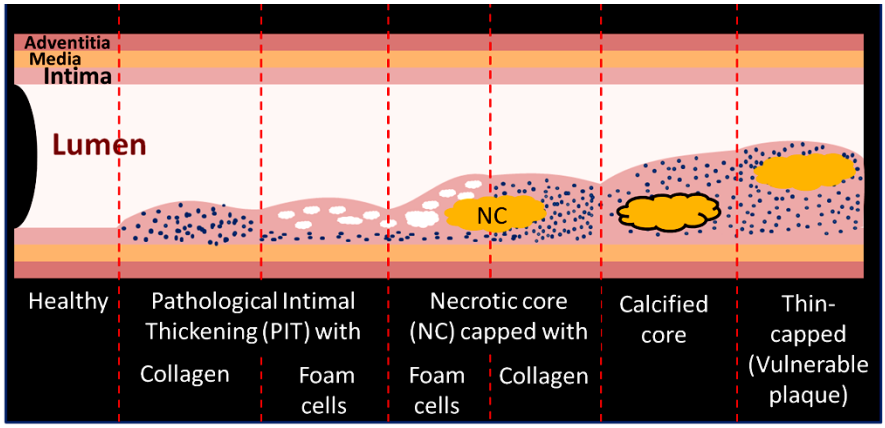

Figure 1: Highly simplified cartoon of various state of Atherosclerosis. Figure illustrates the phases of an artery from when it is healthy to when the artery is narrowed. These phases are not necessarily sequential. Different state of the disorder results in different cardiovascular diseases.

Property of light-tissue interaction changes with the modification of the morphology and biochemistry of the tissue [14]. Generally, optical properties of the tissue such as the scattering coefficient and absorption coefficient are influenced due to change in the size, distribution and composition of the particles in the tissue. If a tissue contains autofluorophores, the fluorescence property of the tissue may change due to alteration in their relative abundances. On the other hand, if the non-fluorescing components (molecules) of the tissue are tagged with a fluorescent agent, the fluorescence property of the agent may change depending on the activities of these molecules. Thus, optical imaging modalities, which use the tissue optical response to yield images of the tissue, can be applied for tissue diagnosis.[*]

Some of the optical imaging modalities that probe the morphology of tissue are confocal microscopy and Optical Coherence Tomography (OCT). Likewise, the

[*] Sound-tissue interaction is another phenomenon that Ultra-sound is based on. Ultrasound is used to probe morphology of the sample.

biochemistry of a tissue can be assessed using modalities like multi-photon microscopy, Raman spectroscopy, fluorescence spectroscopy and Fluorescence Lifetime imaging Microscopy (FLIM).

For detailed understanding of a disease, all the available biomarkers need to be investigated as they are inter-related. Unfortunately, no single optical imaging modality is capable of measuring all of the changes in the optical response of pathological tissue. However, a promising solution is to combine two or more individual modalities such that the product contains the strengths of the constituent modalities. As a combined system, such multi-modal diagnostic tools are capable of interrogating the morphology as well as the biochemistry of a tissue. Information obtained with multi-modal systems help in analyzing a disease with improved sensitivity and specificity [15].

Over the years, this strategy has been adopted by many researchers, who have developed multi-modal instruments and have tested their applications. For instance, Raman Spectroscopy (RS) and Intra-Vascular Ultra-Sound (IVUS) have been combined for the study of lipid and calcium packets in atherosclerotic plaques [16]; time-resolved fluorescence spectroscopy has been combined with ultrasonic backscatter microscopy for atherosclerosis diagnosis [17]; Optical Coherence Tomography (OCT) has been fused with RS for tissue characterization [18]; Fluorescence Lifetime Imaging Microscopy (FLIM), photoacoustic and ultrasound have been combined to yield increased sensitivity and specificity in diagnosis of oral cancer [19]; and Full-field Optical coherence microscopy and optically sectioned fluorescence microscopy have been combined for high resolution images of micro-architecture of tissue and its

components highlighted by contrast agents [20]. We can also find examples of combined OCT and multi-photon microscopy [21], OCT and fluorescence spectroscopy [22-28], OCT and multi-photon tomography [29], confocal Raman spectroscopy and confocal microscopy [30], and reflectance confocal microscopy and FLIM [31]. Furthermore, some of the dual-modality imaging tools have also been successfully used in patients in clinical settings [32, 33].

A combined system to be used for the imaging of an oral tissue and an artery requires two main capabilities that are discussed below:

1) The thickness of epithelial layer of oral tissue and the intima of the artery, when diseased, are below 1mm [9, 34]. The system should have imaging depth range that scans this thickness. Within this depth, the epithelium contains several layers with few microns of thickness. Their measurement is needed to understand the condition of the tissue. Similarly, the intima contains areas with several forms of plaques within the imaging depth. These regions may be loaded with foam cells, may be calcification or may contain a necrotic core. The fibrotic cap over the necrotic core has varied thickness and is marked to be vulnerable to rupture if it measures <65μm. Therefore, the imaging system to be used for oral cancer and atherosclerosis diagnosis should have an axial resolution that is sufficient to measure few tens of microns of thickness and a lateral resolution to identify the variation in structures. In short, the system should have the ability to assess morphological changes in tissue up to a depth of 1mm with high resolution.

2) These tissues consist of endogenous fluorophores whose relative abundance changes with the progression of the disease. In oral tissue, such intrinsic or endogenous fluorophores are collagen, NADH and FAD [11, 35-37]. Fluorescence from collagen decreases due to its degradation in stroma and the thickening of the epithelium. Fluorescence from NADH decreases while that of FAD increases with the development of a lesion. Similarly, in arterial tissue, the autofluorophores are collagen, LDL and elastin. Fluorescence from elastin is predominant when the artery is healthy. Artery with pathological intimal thickening has higher fluorescence from collagen. At deposition of foam cells, strongest fluorescence is from LDL. Beside these fluorophores, tissue also has some non-fluorescing biochemicals of interest (which have been studied with other modalities [38-40]). These molecules can be studied by tagging them with a dye. The system should be able to probe the emissions from all the endogenous and the exogenous fluorophores.

OCT and FLIM are two modalities that meet these requirements. OCT is a high speed optical imaging modality that non- or minimal-invasively provides 2-D and 3-D morphological images of a tissue up to a depth of few millimeters. It has better penetration depth than that of confocal microscopy and better axial resolution than that of an IVUS system. It has axial resolution of few microns and lateral resolution of few tens of microns, which are adequate to distinguish layers and to identify patterns in the tissue. Study shows that OCT is able to discern changes in the epithelial and sub-epithelial layers of the oral tissue [7-10, 41]. OCT images also report thickness of intima, location and thinness of fibrotic cap, and the size and structure of the necrotic core [42-

46]. Introduction of OCT to atherosclerosis diagnosis has enabled detection of smaller pools of lipid in coronary artery, which could not be identified with IVUS [47]. On the other hand, FLIM provides information on tissue biochemistry based on the characteristics of the emissions (endogenous as well as exogenous) from the fluorophores: wavelengths, intensities and lifetimes. FLIM collects emissions from all the fluorophores simultaneously and separates them spectrally. The resulting emission signals are used to calculate the intensity and lifetime for each fluorophore. Intensity provides the relative concentration of the fluorophore. Lifetime accurately identifies the fluorophore and its environment. Each fluorophore has a distinct lifetime for a given environment and emission wavelength. For example, at a range of 500-550nm, LDL and elastin have similar emission spectrum as shown in Figure 10; however their fluorescence lifetimes are ~10ns and ~4ns, respectively. Likewise, free and bound NADH molecules have fluorescence lifetimes of ~0.5ns and ~2-3ns but similar emission spectrum with maximum emission at 450nm. Therefore, even if the emission spectra of two fluorophores or a fluorophore in different environment overlap, the lifetime of the acquired emission helps in determining the source of emission and its environment. Thus, such multi-spectral FLIM support simultaneous acquisition of emissions from a group of any fluorophores as long as their lifetimes are different. This is the advantage of FLIM over fluorescence spectroscopy, which characterizes emissions just based on their wavelength and intensity. Various FLIM systems have been designed to acquire emissions from the autofluorophores in oral tissue [48-50]. Their results demonstrated a difference in the intensities and lifetimes of the emissions between normal and

pathological tissue. Similarly, research on the application of FLIM in arterial imaging evaluated the emissions from elastin, LDL and collagen for classification of the stages of atherosclerosis [51-53].

From the discussion above, it is evident that OCT and FLIM are two imaging modalities that are suitable to image oral tissue and arteries. A general hypothesis for the development of a combined system with these two modalities is that the combined images obtained from the system improve the sensitivity and specificity for the detection of all stages of the disease as compared to individual OCT and FLIM images. The high resolution OCT images help in quantifying various characteristics of the tissue structure (e.g. thickness, depth, shape of the margins, texture) that can be associated with a condition of the tissue. Multi-spectral FLIM images, on the hand, delineate the chemical composition of the tissue in terms of the emission intensities and lifetimes. Using a combined image, the morphological and biochemical information can be merged to get a better understanding of the tissue, hence increasing the sensitivity and specificity in disease classification.

1.2 Objective and dissertation outline

The goal of the project is to develop a novel dual-modality system with OCT and FLIM and to test the system's application on the diagnosis of oral cancer at an early stage and atherosclerosis *in-vivo*. These aims are achieved in stages.

To begin, a high resolution synchronized bench-top prototype of an OCT-FLIM system is designed and developed. The OCT subsystem is designed to have a scan depth range of about or more than 1mm, a high axial resolution of few microns and a lateral

resolution of few tens of microns. FLIM system is designed to collect emissions from the autofluorophores and/or exogenous fluorophores in the tissue, and has a lateral resolution of few hundreds of microns. As a part of the development, the system is validated using an arrangement that mimics the characteristics of a tissue.

Subsequently, animal model for oral cancer is designed. Hamster is known to have oral epithelium similar to humans [54]. These animals develop oral cancer at its late stage in their cheek pouch within 32 weeks from the day they are exposed to a carcinogen, Benzo[a]pyrene (BAP). Advantage of using this chemical to induce epithelial cancer is that the growth of a malignant tissue is gradual. This allows assessment of multiple stages of oral cancer, including its early stage. These animals treated with BAP are thus imaged in cohorts at different time points within the 32 weeks using the OCT-FLIM system. The data collected are evaluated to interrogate the system's capability to provide morphological and biochemical images that can be correlated to each other and to the corresponding histopathology. Furthermore, these data are analyzed to develop classification criteria for identifying stages of oral cancer. Data are also used to study algorithms for data analysis and for classification automation based on the criteria developed. The hypothesis is that the results evaluate the ability of the algorithm and the combined imaging system to distinguish between multiple stages of cancer, including cancer at early stage, based on the characteristics of the morphology and the biochemistry of the tissue.

Likewise, the bench-top system is used to embark the investigation on the diagnosis of atherosclerosis. Postmortem human arteries are imaged with the system.

Artery samples that are available from adult autopsy cases have a wide variety of plaques. Their morphology and chemical composition remain intact for couple of days after the demise. The OCT and FLIM images of the atherosclerotic plaques were analyzed and the analysis was verified with the corresponding histopathological images. These data are used to develop automated classification for identifying plaques based on their structural and biochemical characteristics on the images. The hypothesis is that the classification of plaques is as accurate as when done by histopathological analysis.

In order to interrogate the application of an OCT-FLIM system on the diagnosis of atherosclerotic plaques *in vivo*, an endoscope is incorporated to it. This endoscopic system is made compact and portable to allow imaging of Watanabe rabbits and swine *in vivo* in clinical settings. The OCT and FLIM images of the plaque are compared to the corresponding histopathological slides.

In addition, non-fluorescing molecules that are vital in atherosclerosis are tagged with exogenous fluorescence tags during intravascular imaging. The intravascular FLIM images of emission from these tags help in understanding the activities of the molecule during the progression of the disease. These images are coupled with the corresponding morphological and endogenous fluorescence images. The relationship among these images is investigated. The hypothesis is that the morphological, endogenous emission and exogenous fluorescence images acquired simultaneously provide deeper insight on the condition of atherosclerotic plaques. Such detailed information assist in selecting an ideal therapeutic strategy specific to the condition.

This dissertation mainly focuses on the design, development and validation of bench-top imaging system with OCT and FLIM. In this dissertation, two acquisition systems are built*:

1) Combined system containing spectral domain OCT (SDOCT) and FLIM with capability to acquire endogenous emission. This system has been named as the first generation OCT-FLIM system in this dissertation.

2) Combined system containing swept-source OCT (SSOCT) and FLIM with capability to acquire endogenous and exogenous emission simultaneously. This system has been referred as the second generation OCT-FLIM system in this dissertation.

The first system is used to image hamster cheek pouch model with oral cancer *in vivo* and post mortem human coronary arteries *ex vivo*. The capacity of these systems to generate complementary morphological and biochemical images simultaneously is tested using the images acquired during these experiments. The second system is used to image post mortem human coronary arteries *ex vivo* as well. As a trial run, this system is also used to image a Watanabe rabbit aorta, which is tagged with a dye, Alexa Fluor 532 [55]. The system's ability to acquire morphology, endogenous emission and exogenous fluorescence simultaneously is evaluated.

Based on the aforementioned objectives, this dissertation has been organized as follows:

Chapter 2 discusses the theory of Fourier-domain OCT (FD-OCT), and FLIM. The first sub-section covers the fundamentals of the two variants of FD-OCT, SDOCT

* Spectral domain OCT and Swept source OCT are two techniques of Fourier domain OCT.

and SSOCT, and their key parameters. The second sub-section focuses on the theory of multi-spectral time-domain FLIM and develops an understanding on the important steps required during data processing.

Chapter 3 explains the design and development of the first generation OCT-FLIM system, and describes how the system performance was validated.

Chapter 4 covers our methodology for testing the application of the first generation OCT-FLIM system on Hamster cheek pouch model and post mortem human coronary artery. This chapter also demonstrates some significant examples of complementary OCT and FLIM images.

Chapter 5 discusses the design and development of the second generation OCT-FLIM system. The following subsection describes the methods used for the validation of system. An example of a post mortem human coronary artery imaged *ex-vivo* using this system has also been discussed.

Chapter 6 discusses some of the improvements and limitations of the system. Insights on the on-going as well as future work of this system have also been included.

Chapter 7 summarizes the dissertation.

Parts of [1] have been taken with permission and have been arranged throughout the dissertation.

2. FUNDAMENTALS OF FOURIER-DOMAIN OPTICAL COHERENCE TOMOGRAPHY AND FLUORESCENCE LIFETIME IMAGING MICROSCOPY

This chapter discusses the theory of Fourier-domain OCT (FD-OCT), and Fluorescence Lifetime Imaging Microscopy (FLIM). The first sub-section covers the fundamentals of the two variants of FD-OCT, spectral domain OCT and swept source OCT, and their key parameters. The second sub-section focuses on the theory of multi-spectral time-domain FLIM and develops an understanding on the important steps required during data processing.

2.1 Fourier-Domain Optical Coherence Tomography

2.1.1 Theory of Fourier-Domain Optical Coherence Tomography

FD-OCT is an interferometric technique that analyzes the interferogram as a function of optical frequencies to retrieve the depth-resolved reflectivity profiles of a sample.

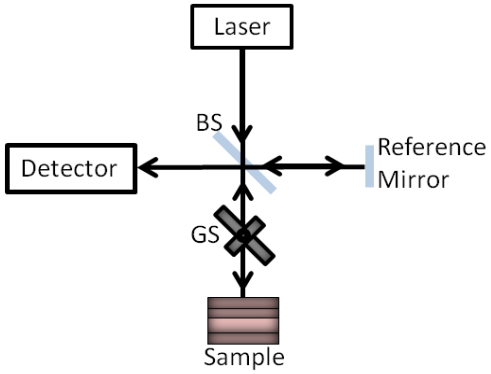

Figure 2: A simple Michelson interferometer based OCT setup. GS-Galvanometer scanner, BS-Beamsplitter. Sample represents a multilayered reflector.

In FD-OCT, a broadband continuous-wave near Infrared (NIR) light is sent through a non-polarizing beamsplitter to form two beams with unequal (for example 90:10, 70:30) or equal (50:50) intensity. Let the source spectrum be $I_i(k)$ with a Gaussian intensity profile, where k is the spatial frequency or wavenumber calculated as $k = \frac{2\pi}{\lambda}$ (λ being the wavelength of the source). Also, let's assume the schematic in Figure 2 splits light into identical beams with intensities $I_i(k)/2$. These two beams travel along two separate arms of the interferometer, the reference arm and the sample arm. The light in the reference arm (with lower intensity in the case of unequal split) is directed towards a fixed mirror, which reflects the light back towards the beamsplitter. Let's suppose, the sample contains N discrete layers, each at a distance of $Z_{S1,}$ $Z_{S2,...}Z_{SN}$. The NIR light in the sample arm penetrates up to 1-2mm into a sample and gets backscattered from multiple layers in the sample (as shown in Figure 2) with intensity proportional to the difference in refractive indices between the layers. This backscattered light from different depths produces optical path length differences between the sample arm and reference arm. i.e. Z_R-Z_{S1}, Z_R-Z_{S2}, and so forth. These path length differences produce interference signals at the detector when the reflected light from the sample and the reference arms are combined at the beamsplitter. These interference fringes are modulated with a frequency proportional to the delay caused by the path length differences.

In FD-OCT, these interference fringes are detected as a function of optical frequencies in two ways. In the first method, known as spectral domain OCT (SDOCT),

a broad band source is used to illuminate the interferometer and the interference signal is dispersed spectrally with a spectrometer. In the second method, called swept source OCT (SSOCT) or optical frequency-domain imaging (OFDI), a broadband source is continuously swept spectrally to illuminate the interferometer with a narrowband light. In this case, the interference signal is detected with a single photodetector in terms of time that corresponds to the wavelength of illumination.

Let $I_R(k)$ be the intensity of the light reflected from the reference arm and $I_{S1}(k)$, $I_{S2}(k)$,...$I_{SN}(k)$ be the intensity of light reflected from each layer of the sample arm, all measured at the detector. Let ρ be the responsivity of the detector.

If the amplitude reflectance of the reference mirror is R_R and that of the layers of sample arm are $R_{S1,}$ $R_{S2...}R_{SN,}$ $I_R(k) = R_R \cdot I_i(k)/4$, $I_{Sn}(k) = R_{Sn} \cdot I_i(k)/4$ where n is the number of reflecting layers in the sample. Here, if $R_R = 1$, $I_R(k) = I_i(k)/4$ since the laser passes through the beamsplitter twice. Let's assume the average refractive index to be n_r.

Interference between $I_R(k)$ and, let's say, $I_{S1}(k)$ is given by,

$$I_{D1}(k) = \rho\left[\left(I_R(k) + I_{S1}(k)\right) + 2\left(\sqrt{I_R(k)I_{S1}(k)}\right)\cos\left(2kn_r(Z_R - Z_{S1})\right)\right] \quad (1)$$

Substituting $I_R(k)$ and $I_{S1}(k)$ with its values in terms of reflectance and $I_i(k)$, we get,

$$I_{D1}(k) = \frac{\rho}{4}\left[\left(I_i(k)(R_R + R_{S1})\right) + 2\left(\sqrt{R_R R_{S1}}I_i(k)\right)\cos\left(2kn_r(Z_R - Z_{S1})\right)\right] \quad (2)$$

In these equations, the factor of 2 in the cosine terms is attributed to the roundtrip pathlength of the sample beam to the reflecting layer in the sample. In other words, z refers to the single pass optical pathlength.

The spectrally resolved signal detected is an integration of interference signal due to every reflecting layer in the sample arm and is represented as:

$$I_D(k) = \frac{\rho}{4}[I_i(k)(R_R + R_{S1} + R_{S2} + \cdots + R_{SN})]$$

$$+ \frac{\rho}{2}[I_i(k)\sum_{n=1}^{N}\sqrt{R_R R_{Sn}}\,cos(2kn_r(Z_R - Z_{Sn}))]$$

$$+ \frac{\rho}{4}[S(k)\sum_{n\neq m=1}^{N}\sqrt{R_{Sn}R_{Sm}}\,cos(2kn_r(Z_{Sn} - Z_{Sm}))] \qquad (3)$$

The first expression in the equation above corresponds to the DC component of the signal (denoted as "DC term"). It represents the components of light reflected from the arms which do not undergo interference. It doesn't contain any information about the location of the reflecting layers in the sample arm. The second expression, called the "cross-correlation term", contains the information on the location and the reflectivity of the reflectors in the sample arm. This is the term that is processed further to obtain the depth reflectivity profile. The last expression, called "Autocorrelation term" represents the interference between backscattered light from different layers on the sample. The term is considered negligible relative to the DC and cross-correlation terms.

The DC term in $I_D(k)$ may be removed electronically. If not, the first step of processing the signal involves "DC subtraction". Intensity of the light reflected from a sample (tissue) is minimal as compared to the intensity of light reflected from the reference arm. Therefore, the DC component of the interferometer is estimated to be the spectrum of the reference arm at the detector when the sample arm doesn't contain any sample. This spectrum is used to subtract the DC component of $I_D(k)$.

Light is dispersed (in SDOCT) or swept (in SSOCT) linearly in terms of λ. Upon conversion to k-space using $k = \frac{2\pi}{\lambda}$, the signal loses its linearity. The cross-correlation term is made linear by interpolation of the signal with a linear array of k. This step is called "resampling". The methods to obtain this linear array in SDOCT and SSOCT have been discussed in sections 3.1.4 and 5.2.6.2 respectively.

To obtain the depth reflectivity profile in terms of z (along the axis of the sample beam), an inverse Fourier transform of the linear interference signal is performed. The Fourier transform of a linear cross-correlation term can then be represented as:

$$\mathrm{I_{int}(z)} = \frac{\rho}{4}\left[\gamma(z) \otimes \sum_{n=1}^{N} \sqrt{R_R R_{Sn}}\, \delta(z \pm 2\mathrm{n_r}(Z_R - Z_{Sn}))\right] \qquad (4)$$

where, $\otimes$ is a symbol for convolution, γ(z) is the magnitude of the Fourier transform of $\mathrm{I_i(k)}$ and $\cos\big(2kn_r(Z_R - Z_{Sn})\big) \overset{F}{\leftrightarrow} \frac{1}{2}\left[\delta\big(z + 2\mathrm{n_r}(Z_R - Z_{Sn})\big) + \delta\big(z - 2\mathrm{n_r}(Z_R - Z_{Sn})\big)\right]$.

According to equation 4, taking inverse Fourier transform of the correlation term, we obtain peaks in terms of ±z, which are delta functions convoluted with the function γ(z). The FWHM of γ(z) determines the axial resolution of the depth reflectivity profile. The amplitudes of these peaks represent the reflectivity of the sample at depth z. Also, in this equation, the peaks get positioned at $2n_r(Z_R\text{-}Z_{Sn})$ while the actual depths are $(Z_R\text{-}Z_{Sn})$. During processing, the positions are calibrated.

One of the properties of Fourier transform is that it is conjugate symmetric, i.e., X(-z) = X*(z). Due to this property, in displaying the Fourier transform of real-valued time function, it is only necessary to display the transform for positive values of z. The resulting depth-resolved reflectivity profile is termed as an "A-line".

In OCT, 2-D and 3-D OCT images are made up of multiple A-lines. Light in the sample arm is used to raster scan the sample using a pair of mirrors controlled by a galvanometer, as shown in Figure 2. Adjacent A-lines from a cross-section of the sample builds a 2-D reflectivity map of that cross-section, called "B-scan". Adjacent B-scans placed together form the 3-D volume of the sample. These B-scans and the subsequent 3-D volume show the morphology of the sample. Further details the theory of FDOCT can be found in general OCT textbooks [56, 57].

2.1.2 Techniques of Frequency-domain Optical Coherence Tomography

2.1.2.1 Spectral Domain-OCT

Figure 3(a) shows a basic schematic of a SDOCT containing the key components. The setup is similar to that of the schematic in Figure 2 except that the free-space beamsplitter is replaced by a 2x2 single-mode fiber (SMF) coupler. In this case, the broadband continuous source is coupled into one port of the fiber coupler and the corresponding output ports deliver split light to each arm. Light from the fiber tips of the ports are collimated and focused onto the respective reflectors. A variable filter is used in the reference arm to control the intensity of the interference signal to avoid saturation at the detector. Light reflected/backscattered from each arm are coupled back into the fibers. The coupler combines them and delivers the interference signal to the spectrometer. A spectrometer collimates the signal and disperses it with a transmitting or reflecting grating. The resulting fringes in terms of wavelength are focused with a compound lens on to a line-scan camera.

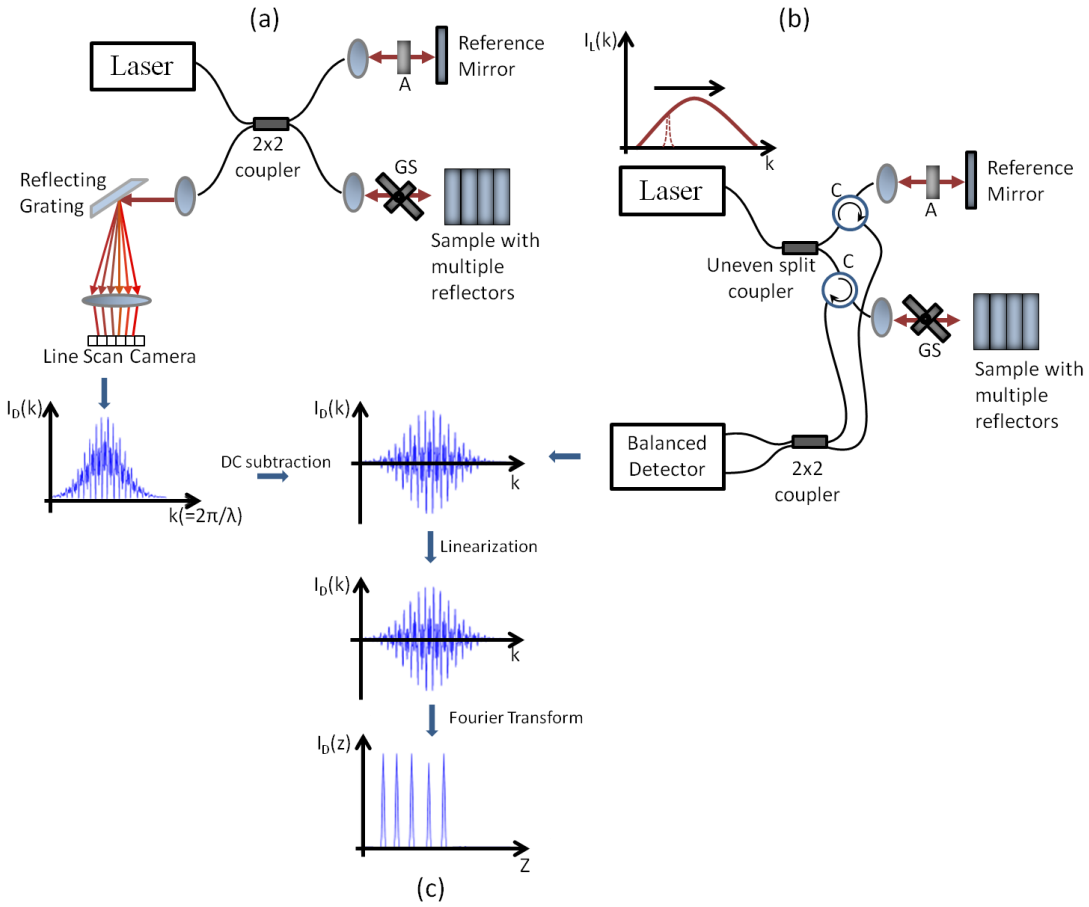

Figure 3: Basic schematic of Frequency-domain OCT. (a) Michelson Interferometry design of a fiber-based Spectral Domain OCT with spectrometer (b) Mach Zehnder Interferometry design of a fiber based Swept source OCT with a wavelength swept laser (c) Process to obtain depth reflectivity from interference signal. A- Attenuator, GS-Galvanometer scanner, C- Circulator.

Signal acquired contains autocorrelation, DC and interference terms as described by equation 3. Autocorrelation is ignored as the signal is weak and the DC signal is subtracted. The remaining interference signal is resampled as described in section 3.1.4. The resulting linear signal is Fourier transformed to obtain an A-line. Figure 3(c) shows the important steps of processing in SDOCT just discussed. The sample in the figure

contains 5 reflecting surfaces and the resulting A-line shows corresponding peaks at different depths along the axis of light penetration.

2.1.2.2 Swept Source OCT

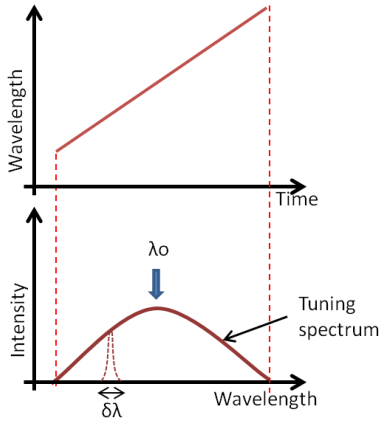

Figure 4: Tuning mechanism of Swept source Laser

In general, a Swept source OCT system contains a broadband source whose wavelength is swept continuously at a certain repetition rate to emit narrowband spectrum with instantaneous line-width (FWHM), δλ, as shown in Figure 4. The broadband spectrum of the laser is the tuning spectrum. Sweep is mostly linear in λ, though some lasers are designed to be linear in k-space [58]. The sweep direction is either uni- or bi-directional. Similar to SDOCT, the swept source is coupled into an interferometer. Interference signals for each narrowband of wavelength is integrated and detected with a balanced detector over time.

Figure 3(b) shows an example of a Mach Zehnder interferometer setup of SS-OCT. Here, source is split unevenly and higher intensity light is delivered to the sample

arm through circulators. Light reflected/backscattered from each arm interfere at the 2x2 SM coupler. A balanced detector acquires the interference signal over time, filtering the DC electrically.

This signal can be considered analogous to the interference signal in SDOCT after DC subtraction. Each narrow spectrum during a sweep of the laser is associated with a sample point of the signal. The interference signal can thus be viewed to be in terms of λ or k.

Similar to SDOCT, signal is then re-sampled in k-space. Distribution of the signal in terms of k is not linear due to non-linear sweep in k and can be made linear using several techniques [59-61]. The method used in this project has been discussed in section 5.2.6.

The remaining steps to process the linear interference signal to retrieve the A-line is the same as that of SDOCT, as shown in Figure 3(c).In general, the FWHM of Fourier transform of the tuning spectrum, provides the axial scanning resolution. During data processing, windowing may be applied to the spectrum (as described in section 5.2.6.2) such that the FWHM of the Fourier transform of the resulting spectrum is the axial resolution.

2.1.3 Figures of Merit

2.1.3.1 Wavelength

Penetration depth of light depends on the absorption and scattering coefficients of the medium. Values of these coefficients vary with the wavelength of light. This infers that the penetration depth depends on the wavelength of the light. Since one of the

factors that determine the performance of OCT is penetration depth, it is important to understand the optical properties of the sample and to choose the best operating wavelength accordingly.

Optical window for biological sample ranges from visible light to NIR. Absorption coefficient is the least and light attenuation occurs mainly due to scattering in this window. Light used for OCT has wavelength in this range. Furthermore, choice of the operating center wavelength lies on the application of the system. For example, OCT uses light at 800nm to image an eye in order to minimize signal degradation due to absorption by the aqueous humour. However, OCT designed for intravascular imaging uses light with wavelengths longer than 1μm for deeper penetration.

2.1.3.2 Resolution

In OCT, two types of scanning yield a 3D structural image: an "A-scan" (axial scan) and a "B-scan" (lateral scan). Therefore, axial and lateral resolutions are two important parameters in OCT. Resolution define the distance between two points that can be easily resolved. Based on Rayleigh criterion, the full width at half of maximum intensity (FWHM) of the point spread function measures the resolution of the system.

Axial resolution is the resolving ability along the axis of the beam in the sample. Axial resolution is measured as the FWHM of the function derived by taking the Fourier transform of the source spectrum in terms of k. Theoretically, assuming the source spectrum has a Gaussian distribution with spectral band width $\Delta\lambda$ (FWHM of the spectrum) and center wavelength of λ_o (which is equal to $2\pi/k_o$), the axial resolution is calculated as:

$$\delta_z = \frac{2\ ln2}{n\pi} \times \frac{{\lambda_o}^2}{\Delta\lambda} \quad (5)$$

Here, n is the refractive index of the medium between the sample and the lens. From the equation, we can infer that axial resolution is inversely proportional to the bandwidth of the spectrum. Therefore, in OCT, use of a broadband source provides better axial resolution. Axial resolution for a typical source like superluminescent diodes (SLDs) is about 5-8μm and can be improved by using femtosecond lasers.

Lateral resolution, δ_x, on the other hand, is the resolving ability in the directions orthogonal to the beam axis. Based on Rayleigh criterion, it is the FWHM of the beam focused at the sample. In general, lateral resolution of an OCT system is few tens of microns.

2.1.3.3 Depth of focus

The other important parameter in OCT is the Depth of Focus (DOF). While focusing a beam, its spot size is the least at the focal plane ($Z = 0$). Here, spot size means the radius of a Gaussian beam waist on the plane (x-y). Let the radius of beam be w(Z). The minimum radius at z=0 is then w(Z)=w(0)=w_o. When w(Z) is $\sqrt{2}.w_o$, $Z = Z_{Rayleigh}$, which is known as the Rayleigh range. Depth of focus is $2Z_{Rayleigh}$, $Z = 0$ being the center of the range. This is basically the range of depth where the light can be considered to be "in focus" and backscattered light from this range is useful for an image. Depth of focus of an OCT system can be calculated as,

$$2\ Z_{Rayleigh} = \frac{2\pi}{\lambda}\ {w_o}^2 \quad (6)$$

Based on this equation and general Gaussian distribution, the lateral resolution discussed in the previous section can be formulated as:

$$\delta_x = \sqrt{(2\ln 2)} w_o \tag{7}$$

We should note that DOF is directly proportional to the lateral resolution of the system. This means when the resolution is improved, the DOF worsens and *vice versa*.

2.1.3.4 Sensitivity, roll-off and maximum depth

Sensitivity is another important parameter that denotes the largest permissible signal attenuation within a sample that can still be distinguished from noise. It can be defined as the ratio of signal power generated when a mirror is used as a sample to the weakest signal power equivalent to noise of the system. Sensitivity is also termed as Signal-to-Noise ratio (SNR). SNR of an FDOCT system can be estimated as:

$$SNR = \frac{\rho S_S R_S \Delta t}{2e} \tag{8}$$

Here, ρ is the responsivity of the detector, S_S is the sample illumination power, R_S is the reflectivity of the sample arm, e is the electronic charge and Δt is the detector integration time in SDOCT or the sweep time in SSOCT [62]. Equation 8 provides the achievable SNR of the OCT system.

In FD-OCT, another vital parameter associated with sensitivity is the roll-off. It defines the depth in the sample where the signal sensitivity reduces to half of the maximum sensitivity. Typically, roll-off is few millimeters. In SDOCT, the pitch of the linescan camera of the spectrometer is finite. As a result, each pixel acquires the integration of multiple wavelengths providing a finite spectrometer resolution, $\delta\lambda_{SD}$. Likewise, in SSOCT, the bandwidth of the narrowband spectrum, δλ in Figure 4, is finite. The interference signal detected is thus a convolution of the actual interference

signal and the Gaussian function with FWHM equal to $\delta\lambda_{SD}$(SDOCT) or $\delta\lambda$(SSOCT). Taking the Fourier transform of such signal results in an A-line which is multiplied by a Gaussian function with a FWHM equal to the coherence length. Roll-off is half of the coherence length. Moreover, the spectral sampling interval is inversely proportional to the maximum depth of acquisition. The spectral sampling interval is defined by the number of pixels on the linescan camera in SDOCT and the sampling rate in SSOCT. Thus, better spectrometer resolution and larger number of pixels in SDOCT, and better narrowband spectrum resolution and sampling rate during signal acquisition in SSOCT can improve roll -off and maximum depth.

2.1.3.5 Imaging speed

Imaging speed is crucial when motion artifact during *in vivo* application of the system need to be avoided or minimized. It is determined by the rate of A-line acquisition. In FD-OCT, speed is limited by the read-out rate of the detector (SDOCT) or the sweep rate of the laser (SSOCT).

2.2 Fluorescence Lifetime Imaging (FLIM)*

Upon excitation, some chemicals (fluorophores) emit light. FLIM is a fluorescence spectroscopy technique that collects emission from a sample and characterizes the contents based on the emission properties: wavelength, intensity and lifetime.

---

* Concept and formulation in this section are based on [63] J. R. Lakowicz, *Principles of fluorescence spectroscopy*, Third ed.: Springer Science & Business Media, 2006.

In this section, the fundamentals of fluorescence have been described briefly in section 2.2.1. Section 2.2.2 elaborates the concept of lifetime and the last section covers detailed description of multi-spectral time-domain FLIM.

2.2.1 Basics of Fluorescence

During its interaction with photon(s), an electron of a molecule in its lowest energy level, E_0, (ground state) absorbs energy of the photon to go to one of its higher energy levels, E_m (excited state). A molecule gets excited only when the energy of the photon matches with the difference between two levels, i.e.:

$$\text{Energy of photon} = h\nu = E_m - E_0 \tag{9}$$

Here h is the Planck's constant and ν is the frequency of the photon. Each electronic level further consists of quantized vibrational levels. Energy of a photon may match the difference between the lowest vibrational level of the ground state and a higher vibrational level of the excited state as well. Thus, photons with a range of discrete energies or frequencies can be used to excite a molecule.

Excited states are not stable and electrons return to the ground state following different mechanisms [64]. The phenomenon of relaxation that is relevant to FLIM is called Fluorescence. In this phenomenon, molecules in the condensed phase that are excited to higher vibrational levels of E_m , generally, relax to the lowest vibrational level of the same electronic state within 10^{-12} s, losing some energy. This non-radiative transition within the vibrational levels is called vibrational relaxation. These molecules then generally return to the ground state within near 10^{-8} s while emitting photons with lesser energy than that of the photons absorbed [63]. In most cases, relaxation occurs

from the lowest vibrational level of the excited state. Moreover, similar to the transition during excitation, molecules may relax to one of the higher vibrational levels of E_0 first and proceed to the lowest level non-radiatively. Therefore, photons with a range of discrete energies or frequencies are emitted. These emitted photons are collected and studied using FLIM.

A simple Jablonski's diagram in Figure 5 illustrates the photoluminescence process. Thick lines represent the lowest vibrational level of that electronic level and the thin lines show rest of the vibrational levels. Blue arrows represent the transition from ground state to excited state upon absorption of energy $h\nu_1$, Red wiggled arrows denote the vibrational relaxation. Green arrows represent the relaxation to the ground state from higher state, emitting photons with energy $h\nu_2$.

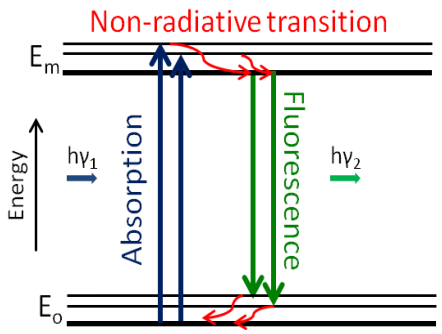

Figure 5: A simplified Jablonski's diagram showing the process of fluorescence. E_0 is the ground state and $E_m$is the excited state. The thick lines represent the lowest vibrational level of the band. The thin lines represent rest of the levels. Figure is color-coded: Blue arrows represent the transition from ground state to excited state upon absorption of energy $h\nu_1$, Red wiggled arrows denote the vibrational relaxation. Green arrows represent the relaxation to the ground state from higher state, emitting photons with energy $h\nu_2$. Electrons relax to higher vibrational levels of E_o. Red arrows on the ground state represent the transition from higher states of E_o to the lowest. Here $h\nu_2 < h\nu_1$.

In equation 9, energy of a photon is directly proportional to its frequency. Since $v = c/\lambda$, where λ denotes wavelength of the photon and c is the velocity of the light, energy can be related to the wavelength of the photon as well. Thus, emission has longer wavelength than that of the excitation light and this property is called Stoke's shift. Additionally, as mentioned before, since a molecule can be excited with a range of energies to emit in a range of energies, the absorption and emission spectra are broad.

The probability of transition from the ground state to each vibrational level in excited state is different. The intensity of the absorption spectrum represents this probability, assuming absence of any other sources of broadening. According to Frank-Condon principle, the probability of a molecule's transition from ground state to the nth vibrational level of E_m is equal to its probability to go from the lowest vibrational level of E_m to the nth vibrational level of E_0. Thus, the absorption and emission spectra of a molecule are symmetrical to each other. Loss-less transition between the lowest vibrational level of E_0 and the same of E_m creates an overlap of these spectra as shown in Figure 6. The excitation spectrum (blue) for Alexa Fluor (AF) is a mirror image of its emission spectrum (green). Shift of the emission spectrum to longer wavelength is due to loss of energy during vibrational relaxation. Further detail on the basic mechanism of fluorescence can be found in [63].

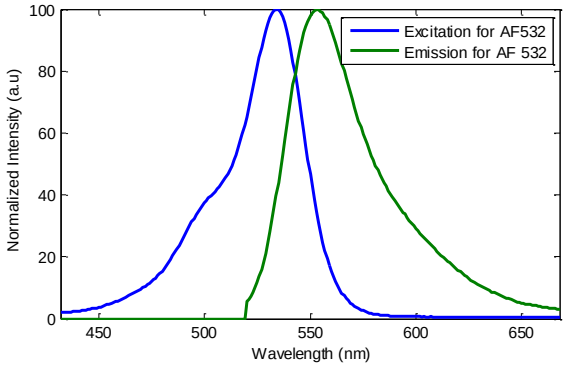

Figure 6: Example of excitation and emission spectra and their properties of Stoke's shift and mirror image. The data for the spectra for Alexa Fluor 532 was taken from [65]. Excitation spectrum (Blue) and emission spectrum (Green) have mirror profiles. The peak of excitation spectrum is at 534nm and that of the emission peak is 553nm. The shift is due to loss of energy in non-radiative transition within the same energy band. This shift is called Stoke's shift.

2.2.2 Lifetime and its estimation

So far, the mechanism of fluorescence has been explained in terms of excitation of an electron of a molecule. In reality, fluorescence involves multiple valence electrons of multiple molecules. Let N be the number of molecules that are in excited state at a given time, t, after incidence of infinitely small width excitation pulse at t = 0s. The rate of relaxation is proportional to the population of molecule in the excitation state, giving us:

$$\frac{dN(t)}{dt} \propto -N(t) \tag{10}$$

If k is the rate constant of the decay dynamics, equation 10 becomes:

$$\frac{dN(t)}{dt} = -kN(t) \tag{11}$$

Also, let's consider the population of excited molecule at t=0 to be N_0. Therefore,

$$\int_{No}^{N(t)} \frac{dN(t)}{N(t)} = -\int_{0}^{t} k dt \text{, or } N(t) = N_0 e^{-kt} \quad (12)$$

Equation 12 can be written as:

$$I(t) = I_0 \, e^{-t/\tau} \quad (13)$$

This is because N is directly related to the intensity of emission. I_o is the intensity of emission at $t = 0$ and τ is the lifetime of emission, which is equivalent to $1/k$. This also brings us to the concept that lifetime is the decay rate of emission intensity and the value can be approximated by measuring the time that the decay takes to reach 1/e of the maximum intensity. Here, equation 13 represents a single exponential decay. However, if there are multiple pathways with different rate constants, the equation denotes a multi-exponential decay.

The above equation is derived also with the assumption that the excitation pulse is infinitely narrow. In reality, the pulse has a width of at least few nanoseconds, causing the decay to be broadened. The resulting decay is the convolution of the true decay and the excitation pulse. Therefore, a method to recover the true decay of the fluorophore is to deconvolve the instrument response function (the response of the instrument to an impulse) from the acquired decay (referred as impulse response function)[63]. The deconvolution algorithm designed for this project was based on a recently proposed and validated Laguerre deconvolution method [66]. This method furnished fast lifetime estimation of multiple fluorescence decays simultaneously. As this dissertation focuses mainly on the instrumentation of the FLIM system, details on the deconvolution algorithm have not been covered. However, for further detail please refer to [67-69].

One other important concept to realize about the estimation of lifetime is that fluorescence emission is a random process in which different molecules in a population emit at different times. Lifetime, τ, is therefore the inverse of the decay rate of the ensemble. In other words, the lifetime we estimate using FLIM is the average time the population spends in excited state. Average time, <t>, either for single or multi-exponential decay, is calculated as:

$$< t >= \frac{\int_0^\infty t.I(t)dt}{\int_0^\infty I(t)dt} = \frac{\int_0^\infty t.e^{(-t/\tau)}dt}{\int_0^\infty e^{(-t/\tau)}dt} \quad (14)$$

When the rate is singular, meaning the decay is single exponential, <t>= τ based on equation 14. For multi-exponential decay, $I(t) = a_1.e^{(-t/\tau 1)}+a_2.e^{(-t/\tau 2)}+...+a_N.^{e(-t/tN)}$, where $1/\tau_1$ through $1/\tau_N$ represent the decay rates. In this case, <t> $\neq$ τ and can be estimated using the equation above.

2.2.3 Multi-spectral Time-domain Fluorescence Lifetime Imaging

2.2.3.1 Optical Configuration

Figure 7 shows a simple schematic of a time-domain FLIM system. It uses a pulsed laser with width narrower than the decay time of the sample as the source for excitation. Excitation beam is focused on a sample. The excitation beam is separated from the emission using a dichroic mirror. Emission is then detected by a Photo-Multiplier Tube (PMT) or a time-gated Intensified Charge Coupled Device (ICCD) camera.

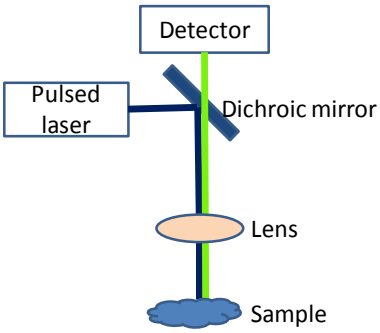

Figure 7: Simple optical setup of a Time-domain FLIM. Blue and green lines represent the excitation and emission beams, respectively.

Tissue is populated with many fluorophores. In such scenario, emission acquired from a confined area of a tissue surface using a FLIM system yields a decay that encodes emission from all the fluorophores in that area. In order to retrieve fluorescence from each fluorophore, the FLIM system described above needs to be modified to a multispectral FLIM system.

A multispectral FLIM system is formed by integrating a set of dichroic mirrors and filters in front of the detector in the setup above. This added setup separates the emission spectrally resulting into channels that provide an impulse response function for a band. For simplicity, let's say the sample has 3 fluorophores and their emission spectra do not overlap. In this case, the dichroic mirrors and filters are set up as shown in Figure 8 and the bands of the 3 channels match with the emission spectra, respectively. The output of each channel is then the decay of the respective fluorophore in the sample. Each channel may be detected with a PMT. However, an economical strategy is to optically delay the channels to form a train of well separated decays that is acquired by just one detector. One way to achieve this is to couple all channels into multi-mode fibers (MMFs) with different lengths and provide the output of the MMF to a detector,

as shown in Figure 8. The difference in the length of these MMFs is given by: $\frac{c \times i}{n_{fiber}}$,

where c is the velocity of light in vacuum, i is the temporal interval needed between the peaks of the decays in the train (value is chosen based on the longest lifetime to be acquired) and n_{fiber} is the refractive index of the fiber, which is approximated to 1.5 for glass during calculation.

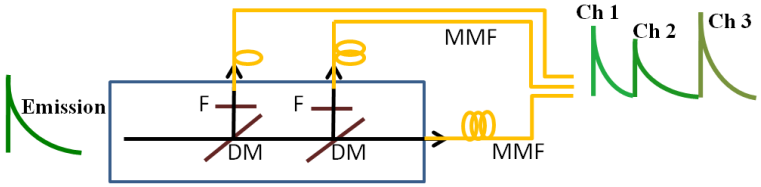

Figure 8: Basic schematic of the setup used to separate the emission spectrally. The combination of dichroic mirrors and filters deliver the emission from each fluorophore to a channel. Each channel is coupled into a multi-mode fiber. These fibers have different lengths such that the decays are detected as a train as shown. DM-dichroic mirrors, F-bandpass filters, MMF-Multi-mode fiber.

Here, we considered a simple hypothetical sample whose emission spectra do not overlap. However, in reality, this may not be true. The next section elaborates on the method of choosing the bands for each channel in either scenario. Section 2.2.3.3 describes how the signal acquired by a multispectral FLIM is processed to obtain the intensity and lifetime of the emission from each fluorophore.

2.2.3.2 Selection of bands for channels

As discussed in the previous section, the fluorophores of interest in a tissue may have emission spectra with no or minimum overlap, making the choice of bands for the channels easy. However, in some instances, the peaks for two fluorophores overlap and

the band has to be picked at the range of wavelength where their lifetimes contrast. This means that one particular channel is designated for both fluorophores and the lifetime helps to identify the source.

In this project, oral tissue and artery were imaged using the systems described in chapters 3 and 5. Oral tissue has fluorophores whose emission peaks are easily distinguishable, and thus is a perfect example of the first scenario above. On the contrary, the second scenario matches with the emissions from an artery. This section elaborates on the choice of bands in each case.

2.2.3.2.1 Oral tissue

The main fluorophores of interest in Oral tissue are Collagen, NADH and FAD. These fluoresce with peaks at ~390nm, ~460nm and ~550nm, respectively, as illustrated in Figure 9. Multispectral FLIM can be adapted to separate the emission into bands based on these peaks. Example of a set of bands is shown with green boxes in the figure.

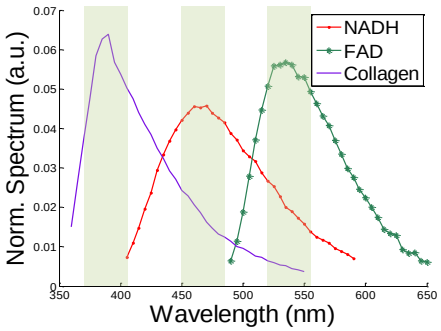

Figure 9: Spectra of Collagen (Purple), NADH (Red) and FAD (Green). The emission peaks of all the fluorophores are distinctly separated. Multispectral FLIM can be adapted to separate emission into the bands indicated by the light green boxes. Data was acquired with a TRFS system*.

* TRFS system used to collect the intensity and lifetime spectra had a general fluorescence spectroscopy setup as shown in Figure 7. The detector contained a monochromator and a PMT.

2.2.3.2.2 Artery

The main autofluorophores in an artery are collagen, LDL and elastin. Figure 10 shows the intensity and lifetime spectra of these fluorophores. In the figure, collagen has peak emission at ~390nm, while both elastin and LDL emit at ~425nm and have similar spectrum shape. Nonetheless, lifetime spectrum of LDL has higher gradient as compared to that of elastin. The center wavelengths of the channels are then around 390nm and anywhere between 480nm to 550nm, respectively. The second channel contains emission from LDL and elastin. Lifetime calculated helps in identifying the fluorophore.

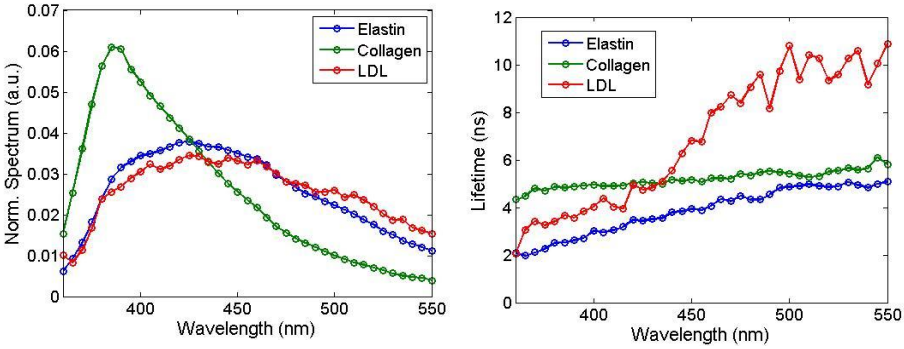

Figure 10: Intensity and Lifetime spectra of emission from collagen (Green), elastin (Blue) and LDL (Red). Data were acquired with a TRFS system.

2.2.3.3 Data processing

Let the number of channels be N in the multispectral FLIM setup. The resulting signal at the detector is then a train of N numbers of decay. Figure 11(a) shows the flowchart of the steps needed to process the signal at the detector. As a foremost step, signal is temporally divided to form a subset of N decays. Each decay is then deconvolved with the excitation laser profile to obtain the corresponding true decay from

the sample. The latter decay is integrated to find the intensity of emission. Equation 14 is used to calculate the lifetime. As a result, N sets of intensity and lifetime values corresponding to N channels are generated. Let these intensities be I_i and the lifetimes be L_i where i = 1,2,3,...N, respectively. Intensity values for the decays are then normalized by the sum of all the intensities, I_1 through I_N, resulting in the corresponding values of I_{n1} through I_{nN}:

$$\text{i.e. } I_{ni} = \frac{I_i}{\sum_{i=1}^{N} I_i}, \text{ where i = 1, 2,...N.} \tag{15}$$

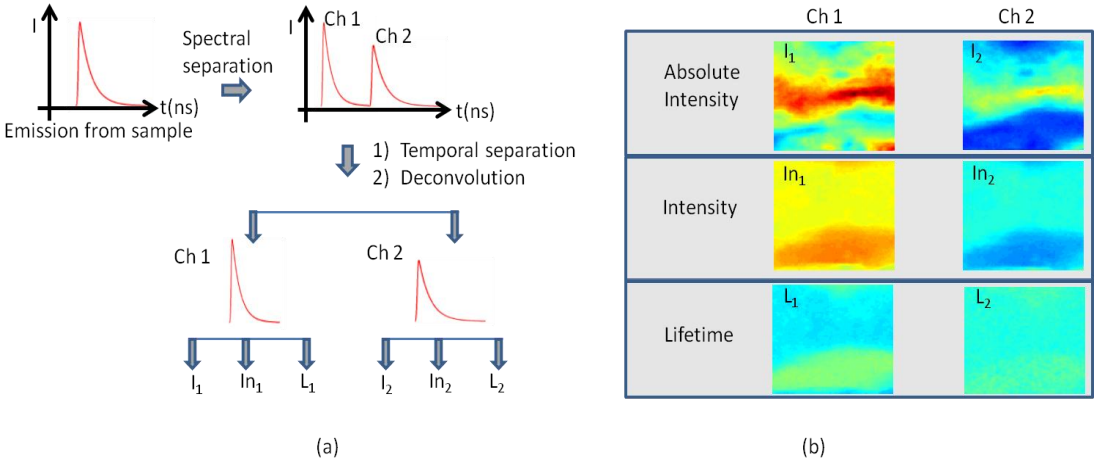

Figure 11: FLIM Data processing with N=2. ch-channel. (a) Emission from a sample is spectrally separated with the multi-spectral FLIM. The signal acquired is thus a train of decays as shown. Following are the steps that are involved in processing this train collected from a single pixel of the sample surface: temporal division to get decay for each band, deconvolution of the decays with the corresponding excitation pulse, and calculation of absolute intensity, normalized intensity and lifetime from each decay (I_1, I_{n1},L_1 for the first band/ch1 and I_2, I_{n2},L_2 for the second band/ch2). Assembling similar information from multiple pixels on the sample, FLIM maps can be formed as shown in (b). (b) A sample of sets of absolute intensity, normalized intensity and lifetimes for each channel.

A typical FLIM system consists of a lateral scanning mechanism, e.g. a galvanometer scanner, to obtain emission from multiple points on the surface of the sample. When a sample is laterally scanned in x-y direction, we get N sets of intensity, normalized intensity and lifetime values for each point (pixel). Assembly of I_1, In_1 and L_1 values for all the pixels form the intensity map, normalized intensity map and the lifetime map, respectively, for the first channel. Repeating the same process for all the channels, we can get similar maps for all the N channels. The total number of maps thus is 3xN. Figure 11(b) shows an example of a set of absolute intensity, normalized intensity and lifetime maps for N=2.

3. THE FIRST GENERATION OF COMBINED OCT-FLIM SYSTEM*

In this chapter, optical design of the first generation combined OCT-FLIM system has been explained. The system was validated by imaging capillary tubes filled with dyes and submerged in intralipid.

3.1 Method

A schematic diagram of the dual-modality imaging system is shown in Figure 12. The diagram can be divided into three sub-diagrams: OCT subsystem, FLIM subsystem, and Common Path. The solid black arrows indicate the optical path of the reference and sample arms of the OCT module. The dashed gray arrows show the FLIM excitation light path, and the solid gray arrows show the FLIM fluorescence emission optical path. The connection between a central computer and all electronics and interfaces is symbolized by a thin solid black line.

* Parts of this section has been taken with permission from [1] J. Park, J. A. Jo, S. Shrestha, P. Pande, Q. Wan, and B. E. Applegate, "A dual-modality optical coherence tomography and fluorescence lifetime imaging microscopy system for simultaneous morphological and biochemical tissue characterization," *Biomed Opt Express*, vol. 1, pp. 186-200, 2010. Copyright by The Optical Society.

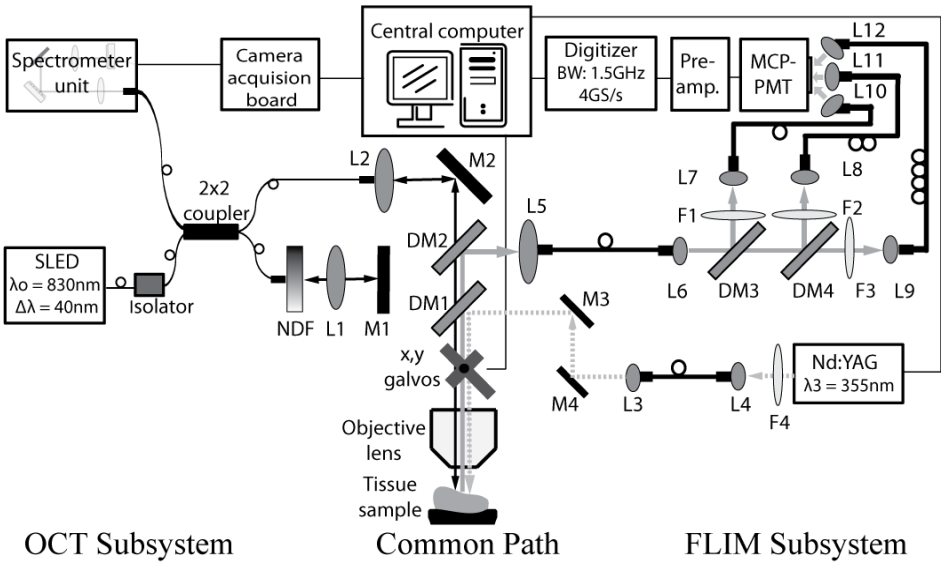

Figure 12: Schematic diagram of the dual-modality imaging system. L1, L2 and L5: free-space collimation and coupling lenses, L3, L4, L6-L12: fiber-connected collimation and coupling lenses, NDF: neutral density filter, M1-M4: mirrors, DM1-DM4: dichroic mirrors, and F1-F4: filters. Dashed light gray lines show the path of 355nm laser, Light gray saolid lines are the emission, and black lines trace the optical path of OCT. Reprinted from [1].

3.1.1 OCT Subsystem

A fiber-based Fourier domain OCT system was implemented as the OCT module. The light source was a superluminescent light emitting diode (SLED) (EXS8410-2413, Exalos, Langhome, PA) with a center wavelength of 830 nm and spectral bandwidth of 40 nm, providing a coherence length (or axial resolution) of 7.3 μm in air. The SLED light propagated into an isolator (AC Photonics, Santa Clara, CA) designed to protect the light source from unwanted back reflections. Light exiting the isolator through single-mode optical fiber (AC Photonics, Santa Clara, CA) was divided by a 2x2 (50/50) single-mode coupler (AC Photonics, Santa Clara, CA) and directed to the reference and sample arms. The reflected beam from a reference mirror in the reference arm and the backscattered light from the sample were recombined at the

coupler and generated a spectral interferogram on a custom designed high-speed spectrometer. The spectrometer was based around a transmissive grating (1200 L/mm, Wasatch Photonics, Logan, UT) and a CCD linescan camera (Aviiva, SM2CL1014, EV2 Technologies, Essex, England) capable of lines rates of up to 53 KHz. The detected signal was digitally converted and acquired by a high speed imaging acquisition board (PCIe-1427, National Instruments, Austin, TX). The OCT subsystem had a signal-to-noise ratio (SNR) of 98 dB and a 3 dB single sided fall-off of 900 µm. The sample arm of the interferometer is encompassed in the Common Path in the OCT/FLIM System will be described in detail in section 3.1.3.

3.1.2 FLIM Subsystem

A frequency tripled (355 nm) Q-switched Nd:YAG laser (SPOT-10-50-355, Elforlight Ltd., England) with a pulse width of 1 ns, and maximum repetition rate of 50 KHz was used as an excitation light source. A 50 µm multi-mode fiber delivered the excitation light to the OCT-FLIM Common Path.

The emission light exiting the OCT-FLIM Common Path was directed through a 200 µm multi-mode fiber into a multi-spectral detection module. As described in section 2.2.3, the multispectral detection system contains a set of dichroic mirrors and filters to divide the emission spectrally. In this dual modality set up, dichroic mirrors from Chroma Technology, R405lp followed by 470DCXR sequentially reflected light for the first and second channels. Bandpass filters, FF01-390/40 and FF01-452/45 from Semrock were placed on the path of channel 1 and 2 respectively. The resulting bands for the three channels were 390 +/- 20nm, 452 +/- 22.5nm and >480nm, respectively.

These bands were temporally separated by propagating each band through a different length (1, 10, or 19 m) of multimode fiber with core size of 200μm which imparted a 45 ns time delay between adjacent bands. The emission bands and fiber lengths were selected to detect tissue endogenous fluorophores, such as FAD, NADH, collagen, elastin and lipids. Upon a single pulse excitation, the three fluorescence decays were simultaneously detected by a MCP-PMT with 150 ps rise time (R3809U-50, Hamamatsu, Japan) and amplified using a high-bandwidth pre-amplifier (1.5 GHz bandwidth, C5594, Hamamatsu, Japan). Finally, the sequence composed of the three consecutive decays was digitized at 4 GS/s using a PCI-ADC card (1.5 GHz analog bandwidth, CS14G8 CobraMax, GaGe, Lockport, IL).

3.1.3 Common Path in OCT/FLIM System

The OCT sample beam and FLIM excitation were aligned to propagate together via a dichroic mirror (DM1) (365DCLP, Chroma Technology, USA) which was highly reflective in the UV and transmitted visible-nearIR (NIR) light. The co-propagating beams passed through a set of galvanometer mirrors (6230H, Cambridge Technology, Lexington, MA) used to raster scan the sample. A broadly achromatic (UV-NIR) objective lens (5X/0.16 NA, EC plan-Neufluar, Zeiss, Germany) was used to focus the OCT sample beam and FLIM excitation with lateral resolutions of 13.4 μm for OCT and 100 μm for FLIM. The fluorescence emission was directed into the multispectral detection module by a second dichroic mirror (DM2), which was highly reflective in the UV-visible range and transmitted NIR.

3.1.4 System Control and Data Processing

A Labview (Labview8.6, National Instruments, Austin, TX) based OCT-FLIM data acquisition interface was developed to control the electronics, data acquisition boards and imaging parameters. The program sent synchronized trigger signals to both the FLIM laser and the OCT camera, so that fluorescence decay acquisition at a pixel coincided with the corresponding OCT A-line collection. 2-D FLIM decay data and co-registered 3-D OCT volume data were acquired after a controlled raster scan with two galvanometers, and saved into the central main computer.

Due to the low pulse energy of the current FLIM laser (maximum of 300 nJ at 10 KHz), tissue autofluorescence decays resulting from a single laser pulse excitation had an inadequate SNR. To improve the SNR of the FLIM signal, multiple fluorescence decays at a given pixel were acquired with multiple excitation laser pulses, and the decays were averaged. The FLIM maps of the *ex vivo* human coronary artery and *in vivo* hamster pouch used 20 fluorescence decays to represent one pixel.

Each Fourier domain OCT A-line was derived in the standard way as described in section 2.1.1 using Matlab (Matlab R2007a, The Mathworks, Inc., Natick, MA) and these are the steps:

(1) DC subtraction: As mentioned before, interference signal contains a DC term. At each imaging session, the sample arm is blocked to collect the reflectance of reference arm. This spectrum is used to subtract the DC component of signal.

(2) Data re-sampling: Signal is in terms of wavelength and need to be converted to evenly spaced k-space. Since dispersion is not linear in k-space, values of the spectral

interference signal at equally spaced k need to be generated using interpolation. In order to obtain a linear sequence of values of k, system is calibrated before is application in samples. For this, the spectrometer is illuminated with a source, for example an Argon lamp, which emits at discrete known wavelengths. These emissions appear as peaks at different pixels and provide a power series up to 3rd order for λ over pixels. Using $k = \frac{2\pi}{\lambda}$, the values of k_{min} and k_{max} corresponding to the first and last pixels, respectively, are calculated. Evenly spaced k-space points are then calculated as $k_p = k_{min} + (p-1) \times \Delta k$, p = 1, 2, ..., P, where $\Delta k = \frac{k_{min} - k_{max}}{P}$. P = the number of pixels x the interpolation factor. As mentioned before, values of k_p are used for interpolation.

(3) Fourier transform: Taking the Fourier transform of the calibrated interference signal, A-lines are generated.

(4) Generation of B-scans and Volume: Adjacent A-lines are assembled to form the 2-D B-scan images and the 3-D volume.

The emission intensities and lifetimes in each band at all pixels were calculated by following the steps, aforementioned in Section 2.2.3.3: segregate decays for each band from the decay train, deconvolve decay with the instrument response, integrate deconvolved decay to get the intensity, use equation 14 to estimate the lifetime, and calculate the normalized intensity. Results were a set of intensity, normalized intensity and lifetime maps for each band.

The OCT volume and FLIM maps were fused by overlaying the 3-D OCT volume with 2-D FLIM maps. The fused OCT/FLIM data were rendered using ImageJ (1.42q, NIH, Bethesda, MA).

3.2 Validation using capillary tubes filled with fluorophores in Intralipid

The OCT-FLIM system validation method was based on the technique used to validate the performance of a solo FLIM system reported in [70]. In this method, three capillary tubes filled with fluorophores were imaged and analyzed. The only change required for the new combined system was that these capillary tubes needed to be within a non-fluorescing scattering medium for the OCT to render the layout of the tubes. The following sections describe the model preparation and the results we obtained after imaging it with the OCT-FLIM system.

3.2.1 Sample preparation and Imaging

Three standard fluorophores with known emission spectra and lifetimes were selected to evaluate the OCT/FLIM dual-modality system: POPOP in ethanol (Emission peak = 390 nm, lifetime = 1.2 - 1.5 ns), NADH in PBS (Emission peak = 450 nm, lifetime = 0.3 - 0.4 ns), and FAD in PBS (Emission peak = 540 nm, lifetime = 2.3 - 2.85 ns) [71]. The fluorophore concentrations (0.015 mM in POPOP, 0.5 mM in NADH, and 1 mM in FAD) were chosen such that the peak emission intensity from each fluorophore was comparable. The dye samples were loaded into three quartz capillary tubes (ID = 300 µm, OD = 400 µm, and Length = 2500 µm). The capillary tubes were sealed to prevent leakage of dyes and were collaterally placed in 2% intralipid which is commonly used to mimic tissue light scattering [72]. The capillary tubes were placed ~100 µm

below the surface of the intralipid and imaged. No averaging was performed, since the fluorescence efficiencies of the dyes were high enough even with a single excitation laser pulse at a pulse repetition rate of 30 kHz.

3.2.2 Results

The OCT-FLIM dual-modality system was first validated by imaging three capillary tubes loaded with POPOP, NADH and FAD placed within 2% intralipid (Figure 13). The OCT/FLIM images were acquired with a pixel rate of 30 KHz. Figure 13(a-b) shows a 3-D OCT volume and a 2-D OCT B-scan image of the capillary tubes (2500 (x) x 2500 (y) x 600 (z) μm). The relative scale on the x, y and z axes in Figure 13 were chosen to improve the visualization of the OCT/FLIM image. The circular structure in Figure 13 represents the ends of the capillary tubes, which essentially show up as a void in the typical speckle pattern produced by the intralipid. Moreover, the inner diameter (305 μm), outer diameter (400 μm), the depth position (~100 μm) from the surface and separation distance between tubes (~750 μm) may be gleaned from the structural OCT image.

Normalized fluorescence intensity and lifetime maps are displayed in Figure 13(c-d). The intensity and the lifetime values were calculated within the capillary tubes only, and the averaged lifetime values were calculated only when the normalized fluorescence intensities in each band were greater than 0.1. The capillary tubes containing POPOP, NADH, and FAD could be identified based on their emission strength and lifetime in each band. POPOP in the leftmost tube showed peak emission intensity at 390 nm, and had a lifetime of 1.42 ± 0.01 ns. Likewise, the maximum

emission of NADH in the middle tube was observed at 450 nm, and the lifetime was 0.36 ± 0.01 ns. FAD within the rightmost tube had the maximum emission at 550 nm with a lifetime of 2.47 ± 0.02 ns. The peak emission and lifetimes determined for each fluorophore was in good agreement with the literature [71]. Figure 13(e-f) depicts the fluorescence intensity map (from the 550 nm band) that has been projected onto the surface of the corresponding OCT volume or cross-section.

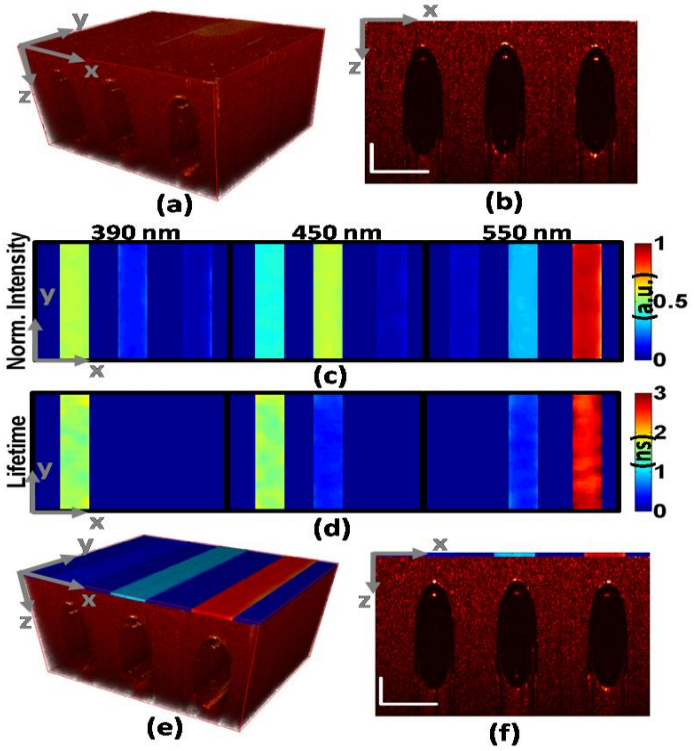

Figure 13: Dual-modal OCT and FLIM images of three capillary tubes loaded with POPOP (left tube), NADH (center tube) and FAD (right tube) within the 2% intralipid (2500 (x) x 2500 (y) x 600 (z) µm). (a) 3-D OCT volume, (b) 2-D OCT B-scan, (c) Normalized fluorescence intensity maps, (d) Fluorescence lifetime maps, (e) 3-D OCT/FLIM volume with fluorescence intensity at the 550 nm band and (f) 2-D OCT/FLIM B-scan image with fluorescence intensity at the 550 nm band. Horizontal scale bar = 500 µm and vertical scale bar = 100 µm. Reprinted from [1].

4. TEST ON APPLICATION OF THE COMBINED OCT-FLIM SYSTEM*

4.1 Introduction

In the previous chapter, the key components of a combined OCT-FLIM were described. The chapter also demonstrated that the OCT-FLIM system efficiently produced the structural and chemical images of the fluorophore filled capillary tubes submerged in intralipid. The first objective of developing the system was to test the application on biological samples ex-vivo or in-vivo. In this chapter, we elaborate the methodology of the experiments, and the results obtained therewith.

The combined OCT-FLIM system was tested on diagnosis of:

(1) Early stage Oral cancer

(2) Atherosclerosis

4.2 Oral Cancer

4.2.1 In vivo hamster cheek pouch model

The OCT-FLIM dual-modality system was evaluated for the early detection of oral cancer lesions using a Syrian golden hamster cheek pouch model of epithelial cancer. Following a previously reported protocol [73], epithelial cancer was induced in 32 animals by treating one cheek pouch of each hamster with a suspension of 2.0% Benzo[a]pyrene (BAP) (Sigma Aldrich Corporation, St. Louis MO) in mineral oil three

* Reprinted with permission from [1] J. Park, J. A. Jo, S. Shrestha, P. Pande, Q. Wan, and B. E. Applegate, "A dual-modality optical coherence tomography and fluorescence lifetime imaging microscopy system for simultaneous morphological and biochemical tissue characterization," *Biomed Opt Express,* vol. 1, pp. 186-200, 2010 Copyright by The Optical Society.

times per week for up to 32 weeks. 22 Control hamsters were similarly treated with just mineral oil. The treatment and imaging protocol was approved by the Institutional Animal Care and Use Committee at Texas A&M University.

4.2.2 Imaging

A cohorts of (3-4) treated and (1-2) control hamsters were imaged every week during the 32 weeks of treatment. For imaging, the hamster was anesthetized with a cocktail of Ketamine (Bioniche pharma USA, Lake Forest, IL) and Xylazine (Akorn Inc., Decatur, IL). After placing the hamster on a small lab jack, the cheek pouch was exposed to the air and positioned under the objective lens of the OCT/FLIM system. Co-registered OCT images and FLIM maps of 2x2 mm^2 tissue sections were simultaneously acquired at cancer-suspicious locations, which were thereafter marked with ink for identification with the tissue histopathology. The heart rate and oxygen saturation of the hamster were continuously monitored during the imaging procedure using a compact veterinary monitor (PC-VetGrad^{+TM}, Vmed Technology, Mill Creek, WA). After imaging, the hamster was euthanized using Nembutal (Hospira, Inc., Lake Forest, IL), and biopsy samples from the imaged locations were taken for H&E histopathology analysis.

4.2.3 Results

Two examples of *in vivo* multimodal imaging of the hamster cheek pouch epithelial tissue are presented here. The first example corresponds to a normal oral mucosa, shown in Figure 14. The second example corresponds to a segment of oral mucosa presenting a squamous cell carcinoma (SCC) lesion, shown in Figure 15.

4.2.3.1 Normal hamster cheek pouch tissue

The OCT volume (Figure 14 (a)) with a size of 2000 (x) x 2000 (y) x 350 (z) µm showed a fairly smooth surface, a blood vessel running at the bottom of the tissue segment, and four discernible layers (Keratinized stratified squamous epithelium (KE), subepithelial connective tissue (lamina propria) (SC), skeletal muscle layer (tunica muscularis) (SM) and adventitial connective tissue (AC) [74]). The position and size of the blood vessel (BV) and the thicknesses of the layers (KE = ~ 20 µm, SC = ~ 80 µm and SM = ~ 140 µm) could also be quantified in the cross-sectional OCT B-scan (Figure 14 (b)), assuming an average refractive index of 1.4. These morphological features were in agreement with the corresponding normal oral mucosa histology (Figure 14 (c)).

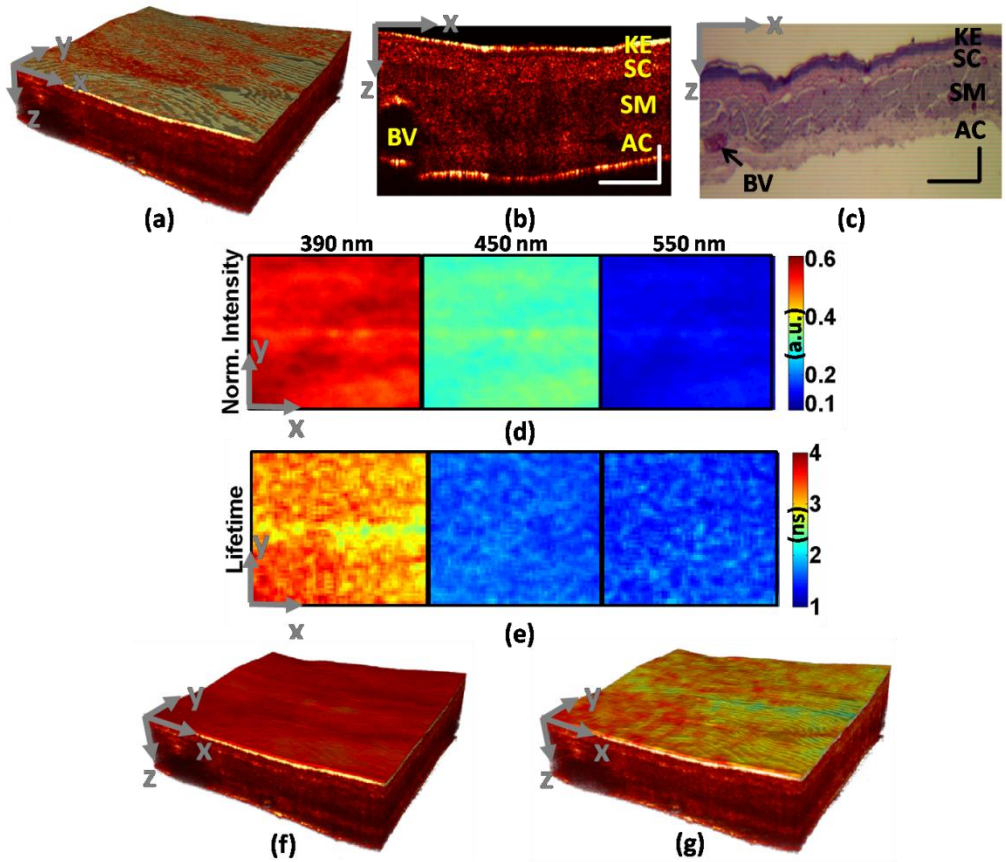

Figure 14: Dual-modal OCT images and FLIM maps of *in vivo* normal hamster cheek pouch (2000 (x) x 2000 (y) x 450 (z) µm). (a) 3-D OCT volume, (b) 2-D OCT B-scan (KE: Keratinized stratified squamous epithelium, SC: subepithelial connective tissue (lamina propria), SM: skeletal muscle layer (tunica muscularis), AC: adventitial connective tissue, and BV: Blood vessel), (c) H&E histology corresponding to (b), (d) Normalized fluorescence intensity maps, (e) Fluorescence lifetime maps, (f) 3-D OCT/FLIM volume with a normalized fluorescence intensity in 390 nm band, and (g) 3-D OCT/FLIM volume with a lifetime in 390 nm band. Horizontal scale bar = 400 µm and vertical scale bar = 100 µm. Reprinted from [1].

Normalized fluorescence intensity and lifetime maps are displayed in Figure 14(d-e). The normalized fluorescence intensity maps were quite homogeneous, with the 390 nm band showing the stronger emission (~ 60%), followed by the 450 nm (~30%) and the 550 nm (~10%) bands; the fluorescence lifetime was longer (~3.5 ns) at the 390 nm band than at the 450 nm (~1.5 ns) and 550 nm (~1.5 ns) bands. These fluorescence

characteristics resemble the emission of collagen, which is the dominant fluorophore in the normal oral mucosa [75].

In Figure 14(f-g) we show the normalized fluorescence intensity and lifetime maps from the 390 nm band overlaid over the corresponding OCT volume of the thin oral mucosa. In these multimodal images, we can clearly see that both the tissue morphology and biochemical composition are fairly uniform within the imaged segment of normal oral mucosa.

4.2.3.2 Cancerous hamster cheek pouch tissue

The OCT volume (2000 (x) x 2000 (y) x 650 (z) μm) in Figure 15(a) showed a major lesion with a size of ~ 1500 (x) x 1000 (y) μm at the bottom and a small tumor-suspicious bump with a size of ~ 200 (x) x 200 (y) μm at the upper right corner. The thickness of the major lesion (~650 μm) and normal-like surrounding area (~250 μm) was visibly determined in a cross-sectional OCT B-scan along the main lesion (Figure 15(b)), assuming the average tissue refractive index of 1.4. Degradation of the layered structures toward the major lesion and no layer at the lesion location was also observed although OCT signal under the major lesion was weak due to low backscattering from the thick cancer lesion. Histopathology analysis of the imaged area confirmed that the major lesion corresponds to squamous cell carcinoma (SCC) (Figure 15(c)).

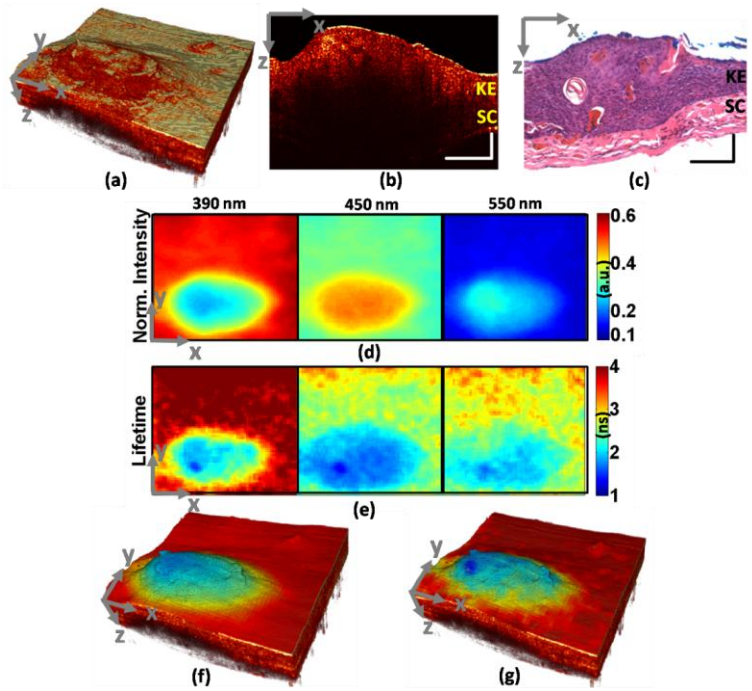

Figure 15: Dual-modal OCT images and FLIM maps of in vivo cancerous hamster cheek pouch (2000 (x) x 2000 (y) x 650 (z) µm). (a) 3-D OCT volume, (b) 2-D OCT B-scan (KE: Keratinized stratified squamous epithelium, and SC: sub-epithelial connective tissue), (c) H&E histology corresponding to (b), (d) Normalized fluorescence intensity maps, (e) Fluorescence lifetime maps, (f) 3-D OCT/FLIM volume with normalized fluorescence intensity in 390 nm band, and (g) 3-D OCT/FLIM volume with lifetime in 390 nm band. Horizontal scale bar = 400 µm and vertical scale bar = 100 µm. Reprinted from [1].

The multispectral FLIM maps of the cancerous hamster cheek pouch are shown in Figure 15(d-e). The difference between the major lesion at the bottom and the surrounding area was detected in both the normalized fluorescence intensity and lifetime maps in all three bands. The normalized fluorescence intensity in the surrounding area was ~55% at the 390 nm band, ~35% at the 450 nm band and ~10% at the 550 nm band. Lifetimes in the surrounding area were ~3.9 ns at the 390 nm band, ~2.4 ns at the 450 nm band and ~ 2.7 ns at the 550 nm band. The normalized fluorescence intensity and the values of lifetimes resembled those of the normal oral mucosa containing collagen as the

dominant fluorophore. In the major lesion, the normalized fluorescence intensity decreases to ~25% at the 390 nm band, and increases to ~ 45% at the 450nm band and to ~30% at the 550 nm band. The values of lifetimes were ~1.5 ns at 390 nm band, ~1.3 ns at 450 nm band, and ~2.1 ns at 550 nm band. The fluorescence characteristics of normalized fluorescence intensities and lifetimes resembled the emission of NADH (at the 450 nm band) and FAD (at the 550 nm band), which are the dominant fluorophores of cancerous tissues [75].

In Figure 15(f-g), we also show the normalized fluorescence intensity and lifetime maps from the 390 nm band overlaid over the corresponding OCT volume of the imaged lesion. In these multimodal images we can clearly see two distinct regions showing very distinct morphology and biochemical composition, which are in agreement with the histopathological characteristics of a squamous cell carcinoma and benign tissue.

4.3 Atherosclerosis

4.3.1 Ex-vivo human coronary artery

A total of 58 postmortem human coronary artery specimens were obtained within 48 hours from the time of the autopsy, according to a protocol approved by the Texas A&M University Institutional Review Board. The artery specimens were longitudinally opened to acquire OCT/FLIM images from the internal lumen side.

4.3.2 Imaging

For imaging, the specimens were placed on a quartz slide to minimize background fluorescence signal, and moistened to prevent it from drying during the

experiment. The imaged artery samples were processed following standard procedures for histopathology analysis.

4.3.3 Results

Two examples of multimodal imaging of human coronary atherosclerotic plaques are presented here. The first example corresponds to a thin fibrotic plaque, and it is shown in Figure 16. The second example corresponds to a thick fibroatheroma presenting a thick fibrotic cap (TFC) overlaying a large calcified necrotic core (CNC), shown in Figure 17.

4.3.3.1 Artery with thin fibrotic plaque

The OCT volume with a size of 2000 (x) x 2000 (y) x 350 (z) μm showed a fairly flat surface and three discernible layers (Fibrotic plaque in Intima (FP), Media (M) and Adventitia (A)) (Figure 16 (a)). The thicknesses of the layers (FP = ~50 μm and M = ~165 μm) could also be quantified in the cross-sectional OCT B-scan (Figure 16 (b)), assuming an average refractive index of 1.4. These morphological features were in agreement with the corresponding plaque histology (Figure 16 (c)).

Normalized fluorescence intensity and lifetime maps are displayed in Figure 16(d-e). The normalized intensity maps reflected a broad emission spectrum covering the 390 nm and 450 nm emission bands, while the fluorescence lifetime maps showed short lifetimes (~2.00 ns) at the 390 nm band and longer lifetimes (~2.37 ns) at the longer emission bands. These features of the autofluorescence emission of the thin fibrotic plaque resemble the fluorescence of elastin found in the media layer. Since the

amount of collagen in the thin plaque is relatively lower than that of elastin in the media, tissue autofluorescence is expected to be dominated by the elastin emission as observed.

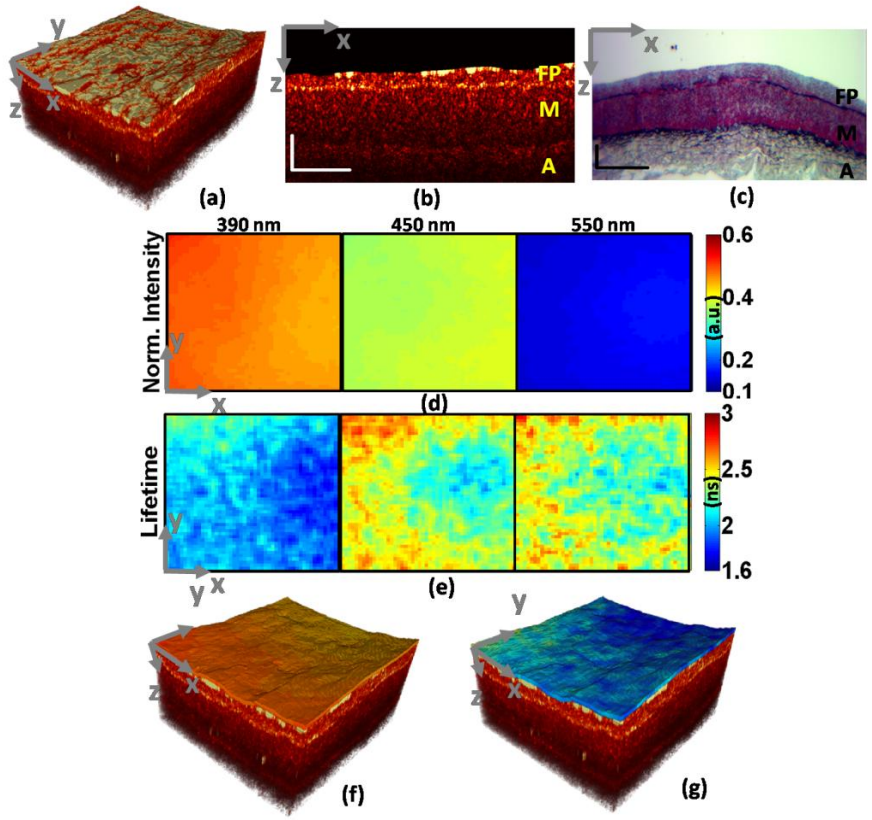

Figure 16: Dual-modal OCT and FLIM images of an ex vivo human atherosclerotic artery tissue with thin fibrotic plaque (2000 (x) x 2000 (y) x 350 (z) µm). (a) 3-D OCT volume, (b) 2-D OCT B-scan (FB: Fibrotic plaque in Intima, M: Media and A: Adventitia), (c) H&E histology corresponding to (b), (d) Normalized fluorescence intensity maps, (e) Fluorescence lifetime maps, (f) 3-D OCT/FLIM volume with normalized fluorescence intensity in 390 nm band, and (g) 3-D OCT/FLIM volume with lifetime in 390 nm band. Horizontal scale bar = 400 µm and vertical scale bar = 100 µm. Reprinted from [1].

The FLIM superficial maps can be superimposed over the OCT volumes to provide a comprehensive characterization of the atherosclerotic plaque. For instance, in Figure 16(f-g) we show the normalized fluorescence intensity and lifetime maps from the 390 nm band overlaid over the corresponding OCT volume. These multimodal

images provide an integrated representation of the underlying morphology and biochemical composition of a thin fibrotic atherosclerotic plaque.

4.3.3.2 Artery with calcified necrotic core

The OCT volume (2000 (x) x 2000 (y) x 650 (z) μm) in Figure 17(a) showed a fairly uniform surface, a large core at the middle of the imaged section, and a thick section towards the right side of the volume. Structural evaluation of the artery tissue was performed on the cross-sectional OCT B-scan image (Figure 17(b)). Averaged thickness of fibrotic cap (~125 μm) and spatial location and extension of the necrotic-core under the cap were clearly assessed based on the backscattering contrast between the cap and the necrotic-core, assuming the average tissue refractive index of 1.4. The corresponding plaque histology (Figure 17(c)) confirmed the morphology of this lesion assessed by OCT.

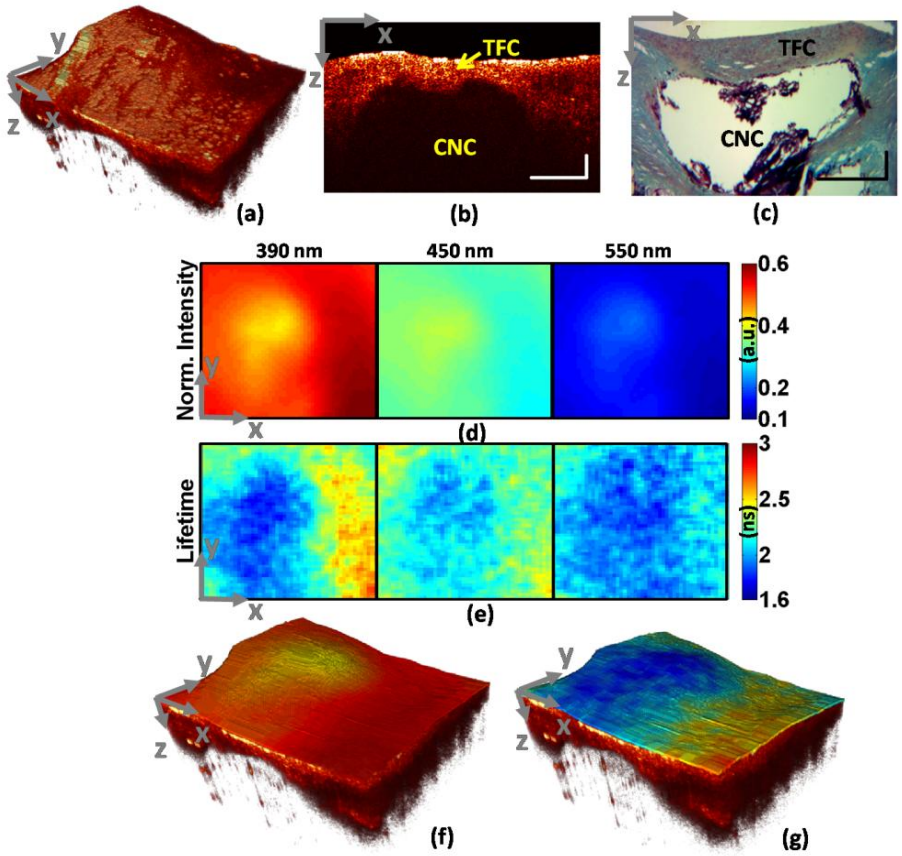

Figure 17: Dual-modal OCT and FLIM maps of an ex vivo calcified human atherosclerotic artery tissue (2000 (x) x 2000 (y) x 650 (z) µm). (a) 3-D OCT volume, (b) 2-D OCT B-scan (TFC: thick fibrotic cap, CNC: calcified necrotic core), (c) H&E histology corresponding to (b), (d) Normalized fluorescence intensity maps, (e) Fluorescence lifetime maps, (f) 3-D OCT/FLIM volume with normalized fluorescence intensity in 390 nm band, and (g) 3-D OCT/FLIM volume with lifetime in 390 nm band. Horizontal scale bar = 400 µm and vertical scale bar = 100 µm. Reprinted from [1].

The multispectral FLIM maps of the normalized fluorescence intensity and the lifetime of the thick cap fibroatheroma are shown in Figure 17(d-e). Two different areas were observed in all FLIM maps that could be correlated to the fibroatheroma region (left) and to a mostly fibrotic region (right). The fibrotic region (right) showed stronger normalized fluorescence emission at the 390 nm band (~ 60%), followed by the 450 nm (~30%) and the 550 nm (~10%) bands; the fluorescence lifetime was longer (~2.6 ns) at

the 390 nm band than at the 450 nm (~2.4 ns) and 550 nm (~2.0 ns) bands. These fluorescence characteristics resemble the emission of collagen, which is the dominant fluorophore in fibrotic plaques [76]. The fibroatheroma region (left) showed similar normalized fluorescence intensities at the 390 nm (~43%) and 450 nm (~37%) bands, and lower intensity at the 550 nm band (~20%); the fluorescence lifetime at all bands were below 1.8 ns. These fluorescence characteristic resemble the emission of lipids, which is abundant inside the necrotic core. [77, 78]

In Figure 17(f-g) we also show the normalized fluorescence intensity and lifetime maps from the 390 nm band overlaid over the corresponding OCT volume of the thick cap fibroatheroma. In these multimodal images, we can clearly see two distinct regions of the plaque showing distinct morphology and biochemical composition, which are in agreement with the histopathological characteristics of a fibroatheroma and a fibrotic lesion.

4.4 Conclusion

The volumetric morphological OCT images and *en face* biochemical FLIM maps of biological tissues measured with the dual-modality instrumentation demonstrate the complementary nature of the two modalities. In the images of the squamous cell carcinoma, the size of the lesion and the breakdown of the tissue layer organization are evident in the morphological image-Figure 15(a-b). The biochemical maps indicate an increased contribution from NADH and FAD (relative to the collagen contribution) in the area of the lesion compared to the surrounding area, likely indicating increased metabolism. Both morphological and biochemical observations are important for

distinguishing a malignant carcinoma from a benign lesion caused by trauma and/or inflammation. Likewise, the morphological image of the atherosclerotic artery in Figure 17(a-b) revealed the existence of a cap over a calcified necrotic core as well as the cap thickness. The biochemical maps Figure 17(d-e) indicated a strong contribution from the structural protein collagen in the area surrounding the fibroatheroma and a strong lipid contribution directly above the necrotic core. Both morphological and biochemical observations are important criterion for classifying the plaque and clinical diagnosis.

5. THE SECOND GENERATION OF COMBINED OCT-FLIM SYSTEM

This chapter discusses the design of the second-generation OCT-FLIM system. This combined system incorporated a Swept-source OCT (SSOCT) and a FLIM is system that was capable of acquiring endogenous and exogenous emission simultaneously. Performance of the new OCT-FLIM system was validated with a capillary tube model as detailed in the section 3.2. Also, the system was validated for its ability to acquire morphology, endogenous emission and exogenous fluorescence simultaneously. Experiments on post mortem human coronary artery as describe in chapter 4 were conducted with this system as well.

5.1 Key changes incorporated in the new system

One of the major changes in the transition from the prior system to the new system was the replacement of the SDOCT subsystem with the state-of-the-art SSOCT system. Michelson interferometry based Fourier domain OCT (FD-OCT) in the previous system that used a super-luminescence emission diode at center wavelength of 830nm was replaced with a Mach-Zehnder interferometry based SSOCT system centered at 1310 nm. With this approach, we achieved improved SNR, penetration depth range and robustness of the OCT system. Introduction of the new SSOCT to the OCT-FLIM imaging system increased the SNR from 98dB to 108dB and the 3dB fall-off from 900 μm to 2.75mm. The depth of focus was increased from .96mm to 3.55mm. However, with the increase in the depth of focus, lateral resolution of the OCT subsystem has been compromised from 13 μm to 32 μm. The new OCT subsystem also attributes improved

stability and portability as compared to the SDOCT as it is mostly fiber-based and doesn't entail a highly sensitive spectrometer.

The first generation OCT-FLIM was capable of acquiring emission from the autofluorophores in the artery. However, many more molecules, which do not fluoresce, play important roles during the progression of atherosclerosis. These molecules can be tagged with a dye whose emission can be collected for their study. In order to accomplish emission collection from exogenous fluorophores, while maintaining the capacity to uniquely identify autofluorophores, we integrated a pulsed 532 nm excitation laser into the system. Autofluorophores get efficiently excited with a short wavelength (355nm in our system) and poorly at 532 nm. This helped in the system's capacity to excite exogenous fluorophores at 532 nm without disturbing the acquisition of the autofluorescence. The pulsed 532nm excitation was interleaved with the pulsed 355 nm excitation. The resulting alternate pulses probed exogenous and endogenous fluorescence, respectively. In this way, the exogenous and the endogenous FLIM images could be obtained simultaneously using a single detector.

Based on the application of the second generation OCT-FLIM system, the multi-spectral emission collection setup described in section 3.1.2 was also modified. FLIM signal is predominantly contributed by elastin in normal arteries, collagen when smooth muscle cell density increases at the artery surface and LDL when foam cells get deposited in the intima of the artery. The prior OCT-FLIM system was specifically designed to probe collagen, bound NADH and FAD to study oral cancer at early stage. Therefore, emission bands were 370-410nm, 429.5-474.5nm and >475nm, respectively.

When used for atherosclerotic plaque imaging, channel 1 provided information on collagen while both channel 2 and 3 yielded the same results on Lipid or elastin. This redundancy was eliminated during the system upgrade by shifting channel 2 to 472-516nm. Also, the dichroic mirror that separated channel 2 and 3 was chosen such that the third channel contained emissions longer than 542nm. Thus, in the second generation OCT-FLIM system, channels 1, 2 and 3 were designed to collect emissions from collagen, low density lipoprotein (LDL)/elastin and exogenous fluorescence, respectively.

5.2 Methods

The new generation of OCT-FLIM optical imaging system, shown schematically in Figure 18, consisted of 4 parts: 1) OCT subsystem, 2) FLIM subsystem, 3) OCT-FLIM common pathway, and 4) Multispectral FLIM collection. The two imaging modalities were optically and electronically synchronized. The free-space optical paths of the beams in the system are color-coded in Figure 18 as: Green-excitation beam for exogenous dye, Blue-excitation beam for endogenous fluorophores, Orange- emission due to 355nm and 532nm, Maroon-1310nm beam path. The thin gray lines indicate connection for trigger.

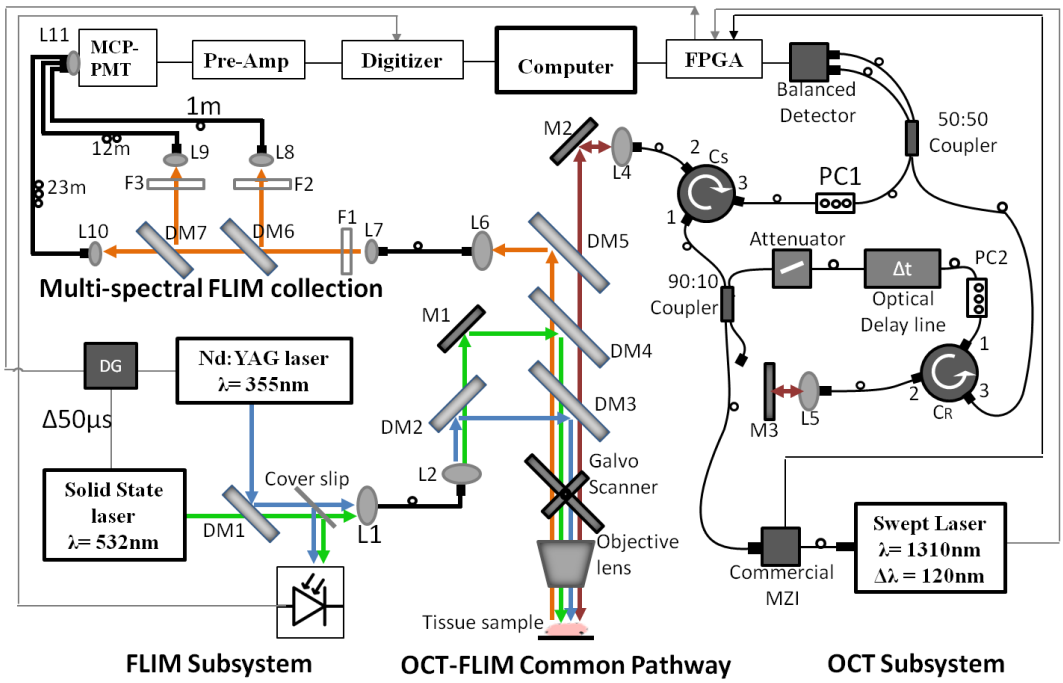

Figure 18: Schematic of the second generation OCT_FLIM system. Green line represents the excitation beam for exogenous FLIM; Blue line is the excitation beam for endogenous FLIM; Orange line is the emission; Maroon line is the beam for OCT; Thin grey line is the trigger path. DM1-DM7:Dichroic Mirrors, L1-L10: Lenses, M1-M2:Mirror, PC1-PC2:Polarization controller, F1-F3:Longpass and bandpass filters, MCP-PMT-Multi-channel plate photo multiplier tube, Pre-Amp-Pre-amplifier, MZI-Mach Zehender Interferometer, FPGA- Field Programmable Gate Array, DG-Delay Generator.

5.2.1 OCT Subsystem

A 1310nm swept source laser (ESS320024-00, Exalos, Switzerland) with bi-directional sweep rate of 100 kHz (uni-directional sweep rate of 50 kHz), tuning bandwidth of 120nm and coherence length of 6mm in air was used for the Mach-Zehnder interferometer based OCT system. OCT beam obtained during rising edge of the sweep trigger (either up-sweep or down sweep) was sent to a commercial Mach-Zehnder interferometer (MZI) (INT-MZI-1300, Thorlabs, USA), whose interference signal provided a reference for spectral linearization [60]. Output beam from the MZI was split with a 90:10, 2x2 single-mode fiber based coupler (10202A-90-APC, Thorlabs,

USA). The end that carried the beam with more intensity delivered light to a free-space setup of sample arm (described in section 5.2.3) through a circulator, Cs. The other end was led to the reference arm of the OCT system. Reference arm begins with a fiber-based attenuator (VOA50-APC, Thorlabs, USA), which is followed by an optical delay line (ODL)(VDL-001-35-60-FC/APC/APC-SS, General Photonics, USA) with length variability of up to 6 cm. The output beam from the ODL passed through a circulator (CIR1310PM-APC, Thorlabs, USA), got collimated by lens, L5, and then focused on a mirror placed at a distance equal to the sample arm's optical pathlength in air. Light reflected from this mirror and the backscattered light from the sample arm were coupled into a 50:50 2x2 single-mode fiber based coupler (NPMC-22-F-13-50/50-FC/APC, General Photonics, USA). Outputs of the coupler were sent to an InGaAs balanced photodetector (WL-BPD600MA, Weiserlab, Germany). OCT signal was digitized with a Labview programmed FPGA (NI PXIe 7966, National Instruments, USA) based digitizer (NI 5772, National Instruments, USA) at sampling frequency of 400MHz. The digitizer and the FPGA were housed in a chassis (PXIe-1082, National Instruments, USA). The Signal-to-Noise ratio of the system was 107db.

5.2.2 FLIM subsystem

A frequency tripled (355 nm) Q-switched Nd:YAG laser (SPOT-10-50-355, Elforlight Ltd., England), pulsed at 10kHz with width of 2ns and maximum energy of 5μJ, was used as the excitation beam for the endogenous fluorophores in the tissue. Likewise, a 532nm solid state laser (1Q532-2, CryLas GmbH, Germany) with a maximum repetition rate of 10 kHz was utilized to excite the exogenous fluorescent dye

tagged to the molecule of interest. Triggers for these lasers were based on the OCT sweep signal (see section 5.2.5), and were configured with a delay generator (P400, Highland Technology Inc., USA) to interleave pulses from the 355nm laser and 532nm with 50μs interval. These beams were spatially combined using a dichroic mirror, DM1 in Figure 18, (425DCXR, Chroma Technology, USA) that reflected 355nm and passed 532nm. A thin quartz coverslip reflected a small portion of light on a photodiode (DET36A, Thorlabs, USA) to generate trigger for the FLIM digitizer at 20 kHz. These excitation beams were coupled into a multimode fiber with a core diameter of 50um (FG050UGA, Thorlabs, USA) to deliver light to the common pathway.

5.2.3 OCT-FLIM common pathway

Excitation beams diverging from the multimode fiber in the FLIM subsystem was collimated. A set of dichroic mirrors maneuvered the collimated excitation lights to co-propagate with the OCT beam. The endogenous and exogenous excitation beams were separated with a dichroic mirror, DM2 (470DCXR, Chroma Technology, USA). 355nm light was reflected with DM2 and DM3 (365DCLP, Chroma Technology, USA) that transmitted everything above 365nm. Similarly, 532 nm light was reflected with a notched dichroic mirror, DM4 (NFD01-532, Semrock, USA) such that the beam travelled together with the 355nm and 1310nm beams. All three beams were directed to a galvanometer scanner (6220H, Cambridge Technology, USA) used to scan sample surface. An achromatic lens (NT64-837, Edmund optics, USA) focused the beams onto the sample, providing a maximum field of view of 16mm by 16mm, and a lateral resolution of 34μm for OCT and 120μm for FLIM. Beam reflected with DM5 (BLP01-

980R, Semrock, USA) was coupled into a multimode fiber of 200μm (BFL22-200, Thorlabs, USA), which delivered light to the multispectral FLIM collection system (described in section 5.2.4). Backscattered NIR light from the sample passed through DM5 and was focused back into the circulator Cs in Figure 18.

5.2.4 Multispectral FLIM collection

A combination of dichroic mirrors, DM6 (R405lp, Chroma Technology, USA) and DM7 (FF520Dio2, Semrock, USA), and bandpass filters, F2 (FF01-390/40, semrock, USA) and F3 (FF01-494_41, Semrock, USA) were used to separate the emission beam into three spectral bands: 390 ± 20 nm (channel 1), 494±22nm (Channel 2) and > 542nm (Channel 3). Emission in channel 1, 2 and 3 were coupled into multimode fibers (BFL22-200, Thorlabs, USA) with a core size of 200μm and varying lengths of 24m, 11.5m and 1m, respectively. The difference in length between the consecutive channels provided an interval of ~60ns between their time-resolved fluorescence emissions at the detector. All 3 fibers were collimated onto the 11mm diameter quartz window of Multi-channel plate photomultiplier tube (MCP-PMT) with 150 ps rise time (R3809U-50, Hamamatsu, Japan). Output of the MCP-PMT was amplified using a high-bandwidth pre-amplifier (C5594, Hamamatsu, Japan) and was digitized at sampling rate of 4 Giga-Sample/s using a PCI-ADC card (CS14G8 CobraMax, GaGe, USA). The digitizer was triggered at 20 kHz with pulses from the photodiode, which was activated by the excitation lasers alternately. Pulse trains at the digitizer due to excitation of 355nm were separated from those due to 532nm excitation and were alternately appended in a file.

5.2.5 System synchronization

Similar to the previous OCT-FLIM system, the two subsystems were electronically synchronized and controlled using Labview (National Instruments, Austin, TX). In this new setup, the internal sweep trigger at 50 kHz was taken as the master clock for the combined system. Beginning of each trigger provided a digital signal to the FPGA to produce synchronized triggers for the OCT signal digitizer, the two mirrors of the galvanometer scanner and the FLIM excitation lasers. Trigger for the 532nm laser was given a temporal shift of 50 μs with a delay generator. The FLIM signal digitizer was triggered by the pulse from the photodiode activated by the excitation beams.

5.2.6 Image Acquisition and Processing

5.2.6.1 Image Acquisition

The optimum number of pixels that each OCT and FLIM images should contain in the x- scan direction and the y- scan direction were determined by the FOV, the lateral resolution of the respective modality, and an oversampling factor of 2. At each pixel, an interference signal and two emission decay trains due to 355nm and 532nm excitations, respectively, were acquired. The SNR of the FLIM signals was improved by spatial averaging. The pulse energies of the FLIM lasers at the sample at 10 kHz were 1.3 μJ (355nm) and 0.9 μJ (532nm).

5.2.6.2 Image Processing-OCT

These were the steps necessary while processing the raw interference signal detected by the balanced detector to obtain OCT images:

(1) Linearization of the fringes: Typically, the tuning of the swept source is not always linear in k-space. Therefore, the interference signal, which is acquired at an equal time interval, has to be subsequently resampled to an evenly distributed k-space by interpolation. The technique for linearization applied in our setup used a reference MZI after the swept laser in Figure 18. Phase of the analytical signal from the MZI was calculated by using Hilbert transform and was then unwrapped. This step assigned each sample point with a value of unwrapped phase. Unwrapped phase obtained in this manner is proportional to k. Linearized phase provided a linear array of k, which was used to resample the interference signal to be equally spaced in k-space. MZI signal recorded during the first sweep was used to resample all the interference signals, assuming that the MZI signal is the same at every sweep.

(2) Numerical dispersion correction: Dispersion that could not be compensated optically was corrected during post processing using a phase correction technique. At the beginning of each imaging session, a mirror was scanned as the sample. The fringe collected encoded the phase difference between the two arms. A phase correction factor that would minimize the difference was calculated. For that, the interference signal from the mirror was recalibrated as described in the previous step and Hilbert magnitude and phase of the recalibrated signal were calculated. Phase was unwrapped and the difference between the unwrapped phase and its linear fit was estimated to obtain the phase correction curve in terms of the sample points.

(3) Windowing and generation of corrected interference signal: Magnitude calculated using Hilbert transform in step 2 represented the laser intensity profile over

sample points. A custom window was generated by dividing a Bartlett-Hanning window by the laser intensity profile. This custom window was then multiplied by the recalibrated signal from step 1 with corrected phase from step 2. As a result, we obtained a dispersion corrected recalibrated interference pattern.

(4) Fast Fourier transform (FFT): FFT of the processed signal obtained from step 3 was taken to obtain the corresponding A-line.

(5) Generation of B-scan and Volume: Steps from 1 through 4 were repeated for the fringes obtained from each pixel of the raw OCT volume data. Adjacent A-lines from each x-direction scan were assembled to form the B-scans. A 3-D matrix containing all the B-scans generated the volume.

5.2.6.3 Image processing-FLIM

Basic FLIM image processing technique used in the first generation OCT-FLIM system was replicated. To summarize the steps briefly:

(1) Fluorescent decay for each band was deconvolved with the corresponding laser function, referred to as instrument response, using Laguerre deconvolution method [66].

(2) Deconvolved decay was integrated over time to calculate the absolute intensity of the emission.

(3) Average lifetime of the decay was estimated using equation 14.

(4) Absolute intensity of endogenous decay in each band was normalized by the integration of intrinsic fluorescent decays in all bands. The third channel was not included during normalization when SNR of the channel was low.

(5) The absolute endogenous intensity maps were calibrated for wavelength-dependent loss in the system using fluorescence decays from Collagen IV (C9879, Sigma-Aldrich, USA) acquired after each imaging session. In order to calculate the calibration factors for each channel, ratio of intensities in each band to that in channel 1 was calculated and compared with similar ratio of calibrated fluorescence intensity obtained using a TRFS system.

(6) Using the steps (1-5), decays in emission bands at all pixels were processed and were assembled to construct 2D maps of normalized intrinsic fluorescence intensities, absolute intensities of endogenous and exogenous fluorescence, and lifetimes as described in section 2.2.3.3

5.2.6.4 Combined OCT-FLIM

FLIM maps were overlaid on top of the OCT volume to simplify pixel-wise, cross-section-wise and volume-wise study of the structure and biochemistry of the sample. Surface of the sample at each pixel in the OCT image was detected by finding the first index in the A-line whose intensity is greater than or equal to the mean plus 2 standard deviations of the mean of the A-line. The intensity values at those indices on the OCT volume were replaced by the values on the FLIM map. Median filters were used for smoothing the detected edges in both x and y directions. Rendering of the overlaid version of OCT-FLIM images was accomplished using a 3-D visualization tool, VTK, based on C++.

5.3 System validation with dye-filled capillaries

5.3.1 Experiment setup

We imaged 3 parallel, coplanar quartz capillary tubes, each filled with a different fluorophore, submerged in diluted milk as a scattering medium for validating the performance of the OCT-FLIM system. POPOP and NADH fluoresce efficiently at 400nm and 500nm, respectively, when excited at 355nm. Rhodamine6G emits at wavelength longer than 550nm when excited with wavelengths both 355nm and 532nm light. Solutions of POPOP in ethanol, NADH in Phosphate Buffer Saline (PBS), and Rhodamine6G in ethanol were prepared to have concentrations of 50μM, 1mM and 2.8μM, respectively. These concentrations were chosen to ensure acquisition of emissions with comparable intensities while using the same amplification on the PMT. These capillary tubes had 0.3mm of inner diameter and 0.4mm of outer diameter. Their ends were carefully sealed before being submerged in diluted milk, which acts as the scattering agent for OCT. This sample was then raster scanned with a field of view of 2.4mm by 2.4mm.

5.3.2 Results

3-D OCT volume and 2-D FLIM intensity and lifetime maps for all three spectral bands were generated. OCT volume was cropped up to the depth where capillary tubes existed, and the normalized intensity was calculated only in the area with the tubes. Lifetimes were calculated only for the pixels whose normalized intensity was greater than 0.2. Since fluorescence from diluted milk was absent, emission from the quartz capillary tubes can be considered purely from the dye within.

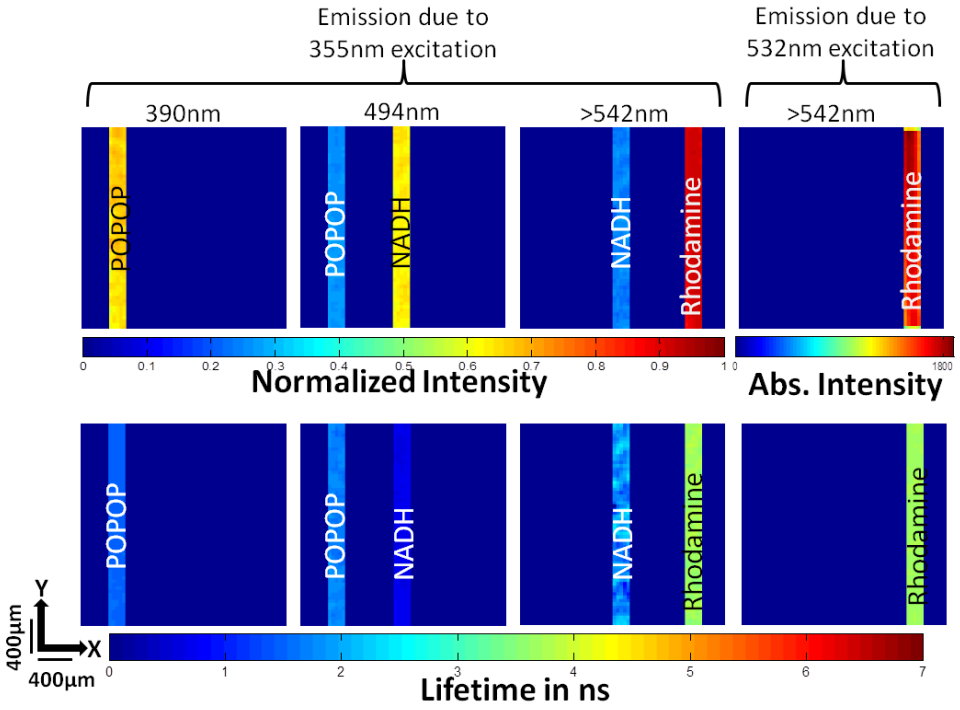

Figure 19: FLIM images of capillary tubes filled with POPOP, NADH and Rhodamine 6G, submerged in diluted milk for scattering. POPOP has maximum peak in channel 1, NADH in channel 2 and Rhodamine 6G in channel 3. Rhodamine 6G emitted when excited with 355nm or 532nm. The lifetimes calculated were: POPOP-1.64±0.06ns, NADH = 0.67±0.04 ns and Rhodamine = 3.72 ± 0.01 ns.

Figure 19 represents the FLIM images (60x60 pixels) that identify the dye inside the capillary tubes. Fluorescence intensity from POPOP peaked in the first channel and that from NADH in the second channel. These fluorophores did not fluoresce when excited with 532nm. Rhodamine6G emitted when excited with 355nm as well as 532nm. Lifetime of POPOP, NADH and Rhodamine6G when excited with 355 nm were calculated to be 1.64±0.06 ns, 0.67±0.04 ns, and 3.72±0.01 ns, respectively. Lifetime of Rhodamine6G was 3.69±0.03 ns when excited with 532 nm. These values were in

agreement with the values found in literature The lifetimes of these fluorophores found in literature were 1.2-1.5ns [71], 0.67ns[50], and 3.99ns[79].

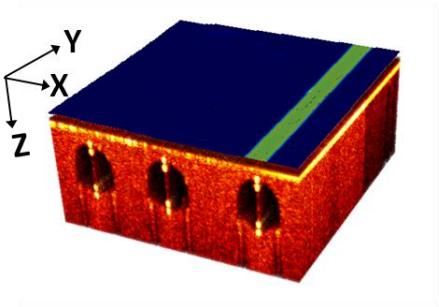

Figure 20: OCT volume of the capillary tubes in milk overlaid with one of the FLIM images. Volume can be overlaid with any FLIM image. The dark circles represent the capillary tube's cross-sections.

Likewise, Figure 20 illustrates a 300 (x) x 300 (y) x 450 (z) pixel OCT volume of the setup. The circular regions with weaker signal represent the cross-section of the capillary tubes while the region with stronger signal denotes light scattered by milk. The diameter of the circle was measured to be 0.4mm, which matched the outer diameter of the tube. Volume in the figure is shown to be overlaid with the lifetime map of channel 3 pertaining to 532nm excitation. Any of the FLIM maps can be overlaid on top of the OCT volume for simultaneous structural and chemical analysis.

5.4 System validation with tissue

Preliminary imaging tests were performed on a non-specifically tagged aorta of a Watanabe heritable hyperlipidemic (WHHL) rabbit *ex-vivo*. These rabbits are animal model that are LDL receptor deficient. They are prone to develop atherosclerotic plaques and show lipoprotein metabolism similar to humans [55]. Alexa Fluor 532 was used as the fluorescent agent.

5.4.1 Sample preparation and Imaging

Aorta removed from the WHHL rabbit was cleaned with PBS and cut open longitudinally. Sample was then cut into two halves, first half being ~10mm by ~10mm (sample 1) and the other ~4mm x ~4mm (sample 2). They were washed with PBS for fifteen minutes by changing the solution every five minutes. A solution of 1% of Bovine Serum Albumin (BSA) (BP671-1, Fisher Scientific, USA) and 0.1% of Tween-20 (BP337-500, Fisher Scientific, USA) in PBS was prepared. A mixture of 1ml of this solution and 5µl of Alexa Fluor 532 goat anti-rabbit IgG (A-11009, Life Technologies, USA) was used to incubate the smaller sample for an hour. BSA helps in blocking molecules to avoid unspecific tagging and Tween-20 enhances the permeability of the tissue. After incubation, tissue was washed with PBS thoroughly. Samples 1 and 2 were raster scanned with the OCT-FLIM imaging system. The 355nm and 532nm excitation beams were interleaved and triggered at a repetition rate of 10 kHz. In order to take the difference in emission intensities between the autofluorophores in the artery and the dye tagged into account, the pulse energy of the excitation beam at 355nm was reduced. SNR of the endogenous fluorescence decay signal was maintained by increasing the number of pixels scanned for spatial averaging. Thus, endogenous and exogenous emissions were simultaneously acquired with a single detector.

5.4.2 Result

Each scan over the entire sample produced an OCT volume, 3 sets of FLIM images that mapped the intensities and lifetimes of the endogenous emissions in 3 bands, and a set of intensity and lifetime maps of the exogenous emission in the third band.

WHHL rabbit endogenous emission in channel 3 was negligible. Therefore, the endogenous emission maps for channel 3 were ignored and have not been shown in the figures.

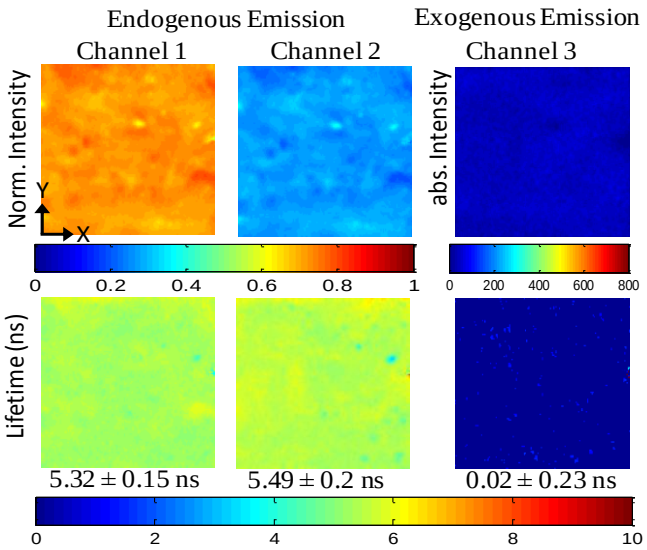

Figure 21: FLIM maps of Watanabe rabbit aorta (Sample 1). Intensity maps in channel 1 and 2 due to 355nm laser excitation suggest predominant existence of collagen. Low signal in the third channel infers absence of any substance on the artery.

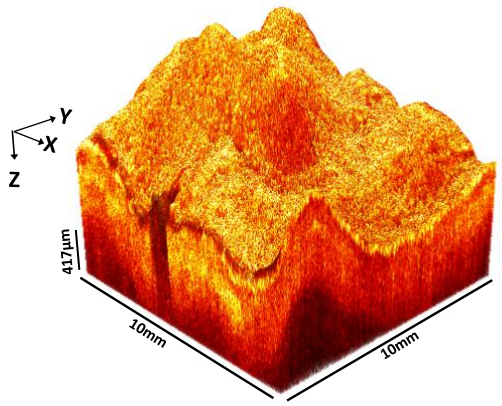

Figure 22: Volume of Watanabe rabbit aorta. Diffused surface indicates pathological intimal thickening.

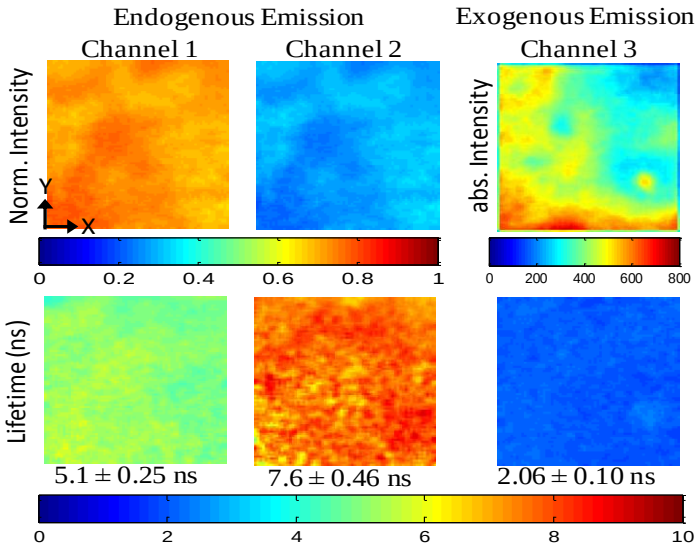

Figure 23: FLIM images of Watanabe rabbit aorta tagged with Alexa Fluor 532 (Sample 2). Intensity maps in channel 1 and 2 due to 355nm laser excitation suggest predominant existence of collagen. The lifetime in channel 2 infers presence of lipid packets within collagen. The lifetime map has a lifetime of 2.06ns which matches with the lifetime of raw Alexa Fluor 532nm. Intensity map in the third channel demonstrates tagging of the dye with different concentration.

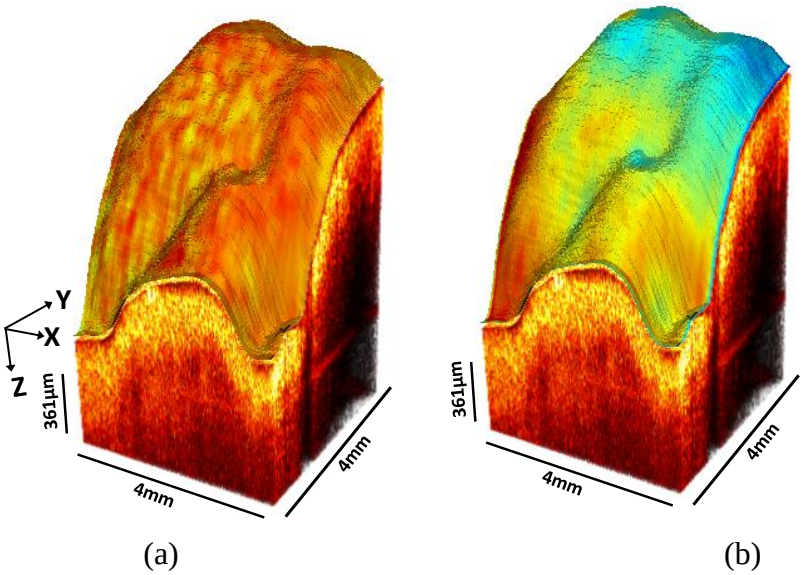

Figure 24: OCT volume of Watanabe rabbit aorta. Strong scattering in the first layer indicates pathological intimal thickening. Volume has been overlaid with (a) Lifetime map in channel 2 (b) Intensity map of exogenous emission. Lifetime in channel 2 indicates lipid packets in the aorta and the intensity map of the exogenous emission signifies success in non-specific tagging of the artery.

Figure 21 through Figure 24 show the OCT and FLIM images obtained from the two samples. Biochemical composition of the surface of the arteries can be analyzed with the FLIM images in Figure 21 and Figure 23. In the first cases, sample 1 (Figure 21), intensity in Channel 1 was higher among the endogenous fluorescence designated channels, suggesting higher concentration of collagen. Similar lifetimes in channel 1 and 2 further confirmed that the emission is mostly from collagen. Normalized intensity maps of Sample 2, in Figure 23, showed pattern of emission similar to sample 1; however, lifetime of 5.1 ± 0.25ns in channel 1 and longer lifetime in channel 2 (7.6 ± 0.46ns) inferred that the sample contained accumulation of lipid scattered throughout the tissue packed with collagen. Channel 3 in each figure indicated the intensity and lifetime characteristics of fluorophore when excited with the 532nm beam. Channel 3 for sample 1 confirmed absence of the dye. The exogenous fluorescence intensity map in Figure 23 showed that sample 2 contained non-specific binding of the antibody conjugated with Alexa Fluor 532 with varied concentration. Uniform lifetime map (2.06±0.1ns) indicated that the dye was conjugated to molecules throughout the tissue. The lifetime of raw Alexa Fluor 532 was measured to be 2.55±0.06 ns. Slight difference in the lifetimes could be due to the change in environment. Figure 22 shows the volume of sample 1; Figure 24(a) shows the OCT volume of sample 2 overlaid with its channel 2 lifetime map, and Figure 24(b) is the same volume but overlaid with the exogenous emission intensity map. The thickened layer in the volume of both samples diffused

homogeneously. Layers of the tissue were not visible, which indicates the presence of pathological intimal thickening.

5.5 Ex-vivo imaging of human coronary artery

The second generation OCT-FLIM system was used to image human coronary artery ex-vivo. We used the same imaging protocol that was used to image human coronary arteries with the first generation OCT-FLIM system. The only difference was the FOV. In the former system, the FOV was 2mmx2mm. With the new system, the maximum FOV was 16mmx16mm and a rectangular FOV was possible. When the specimen had larger area than the system's FOV, it was imaged in parts with few millimeters of overlap. As a result, the system was able to image specimens with circumference as large as 1.2 cm and any length (maximum extracted ~3cm). We have imaged samples from 42 human autopsy cases so far. The sub-sections below describe the preparation method and discuss the OCT-FLIM images obtained from a representative specimen.

5.5.1 Sample preparation

Post mortem human coronary artery was collected and imaged within 48 hours from the time of autopsy. Sample was cleaned with PBS. Unwanted muscle and fat surrounding the artery were removed. Sample was cut open longitudinally. The lumen was imaged with a FOV of 10x11mm^2 that covered 668x734 pixels and 168x368 pixels in x and y directions for OCT and FLIM images respectively. Since the sample was not stained, only endogenous emission was characterized.

5.5.2 Results

Figure 25(a) shows the 3-D rendering of the sample. Using the 3D visualization tool mentioned earlier, the volume can be visualized from different angles. Figure 25(c) illustrates a representative B-scan from the volume. The green arrow shows the location of the B-scan in the volume. For better data visualization and interpretation, the air-tissue boundary of the B-scan can be overlaid with the corresponding FLIM information. Here, the B-scan has been topped with the lifetime values in the second band. Figure 26 depicts the normalized intensity and lifetimes maps for channel 1 and 2. Once again the intensity was normalized by using just the first 2 channels due to poor SNR in channel 3.

Sample has regions with different biochemical composition as indicated by the FLIM maps in Figure 26. For instance, region at the top left denoted by a red square shows higher intensity in channel 2 by a factor of 1.2 while the section marked in purple suggests the opposite by a factor of 1.43. The average lifetime in channel 1 for the red region is 5.47±0.14ns and that in channel 2 is 6.10±0.26ns, showing slight increase in lifetime at longer wavelength. Referring to the trend of intensity and lifetime of the main fluorophores-Collagen, LDL and elastin in Figure 10, we can conclude that the main source of emission is elastin. Likewise, the region in purple has average lifetimes of 6.57±0.07ns and 6.34±0.25ns for channel 1 and 2, respectively. Once again the trend of consistent lifetime and higher intensity in channel 1 tells us that the source is collagen.

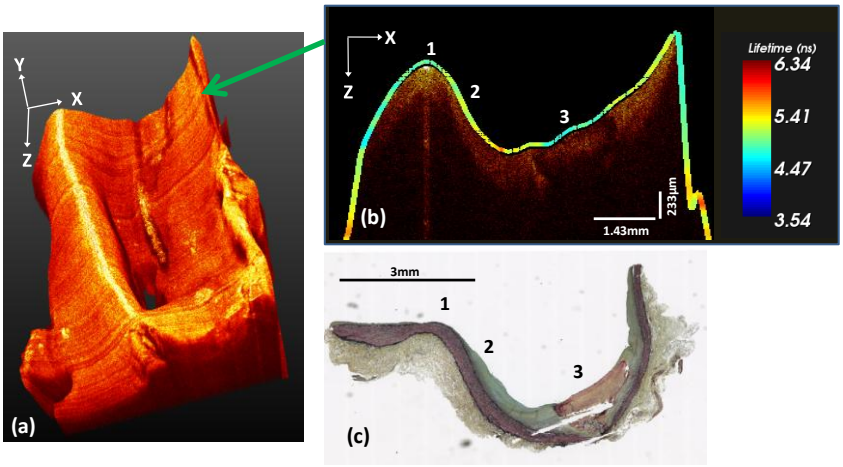

Figure 25: OCT images of human coronary artery. (a) A 3D volume of the artery. (b) A representative B-scan from (a). Green arrow points out where the B-scan belongs to. The surface of the B-scan is overlaid with the corresponding superficial FLIM information. This combination provides us both morphological and biochemical composition of the cross-section. (c) Histopathological image of the artery that corresponds to the B-scan in (b). Regions 1, 2 and 3 in (b) can be compared to the respective regions in (c).

Scrutinizing the structure of the artery in the B-scan in Figure 25, we observe that the leftmost section, marked as 1, has more defined structure as compared to the sloped region, denoted by 2. Region, 3, has defined boundaries with a reflective layer in between, implying that it contains tissue surrounded by calcium. The biochemical information on top clarifies that the tissue in region is predominantly composed of elastin. Additionally, the lifetimes on the surface identifies that the diffused region 2 contains collagen and while region 1 has elastin. The corresponding histopathology section in Figure 25(c) confirms the analysis.

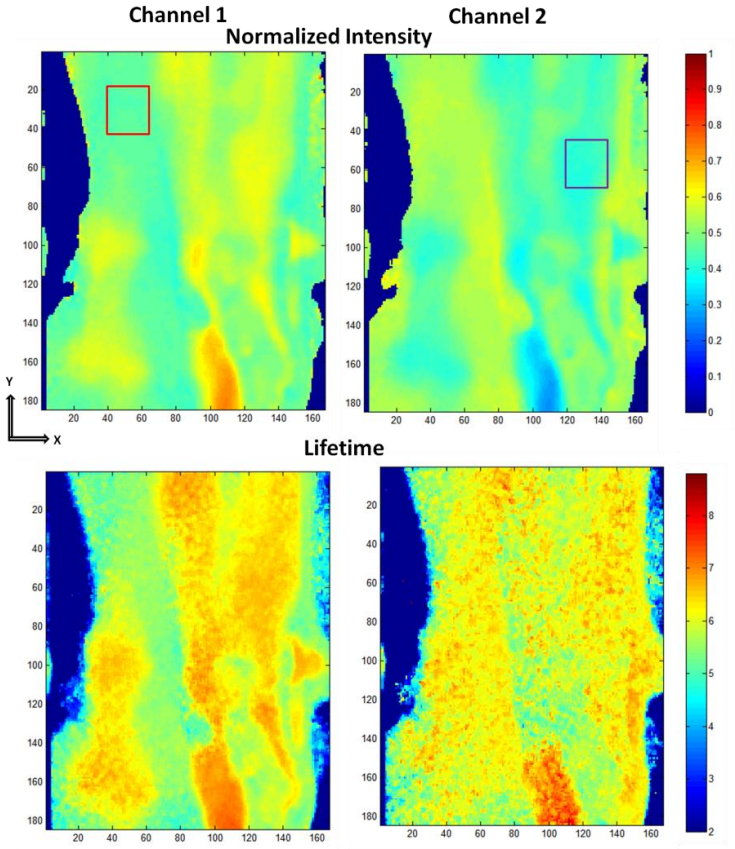

Figure 26: FLIM images of a human coronary artery obtained with the second generation system. The red and purple boxes indicate regions of interest for discussion.

5.6 Conclusion

The latest OCT-FLIM system we built incorporated Swept source OCT for structural imaging, endogenous FLIM system specifically modified for cardiovascular biochemical imaging and exogenous FLIM system that adds capability to image molecules that do not fluoresce. Figure 22 and Figure 24 showed the structure of the aorta and furnished tissue thickness information. Likewise, Figure 23 demonstrated the ability of this multimodal optical imaging equipment to identify lipid content in sample 2 despite the similarity in the morphology of the tissue in Figure 24. Exogenous emission

intensity maps in Figure 21 and Figure 23 distinguish samples with and without treatment of dye. The lifetime map of exogenous emission for sample 2 added confidence that the emission is from Alexa Fluor 532. These results validated the capability of the system to acquire the morphology, endogenous emission and exogenous fluorescence simultaneously.

This system was also utilized in imaging human coronary arteries ex-vivo. An example of OCT-FLIM images of these arteries presented in Figure 25 and Figure 26 appraised the ability of the system to scan large areas, and, once again, the power of the dual modality tool to provide complementary morphological and biochemical information.

6. DISCUSSION

In this dissertation, two dual-modality optical imaging systems were built. The first combined system (the first generation OCT-FLIM system) contained a Spectral-Domain OCT system and a multi-spectral FLIM system for endogenous emission acquisition. The second imaging system (the second generation OCT-FLIM system) comprised of a Swept-Source OCT system and a multi-spectral FLIM system for endogenous and exogenous emission acquisition.

Using the first generation OCT-FLIM system, we imaged hamster cheek pouch model *in vivo* and post mortem human coronary artery *ex vivo*. In this dissertation, only few of the results were presented to support the validation of the systems. Apart from what this dissertation entailed, these data were used for various other studies. Data acquired from hamster cheek pouches were used to test automated classification of OCT images for the diagnosis of oral malignancy [80]. These data are also being used to analyze the application of OCT-FLIM in diagnosis of oral cancer at early stages. The dataset compiled from human coronary artery samples were analyzed to study the significance in characterization of atherosclerosis using FLIM and the combined OCT-FLIM system [81, 82].

Some of the limitations of the first generation OCT-FLIM system were its FOV, OCT depth scan range and the FLIM pixel rate. The maximum possible FOV of the system was $4x4mm^2$. In general, the circumference of an artery ranges from 5mm to 12mm and the entire artery could be scanned only by numerous cumbersome translations

of the sample. Likewise, the laser used for OCT was centered at 830nm wavelength and the system had a fall-off of 900μm. Also, low pulse energy (300nJ per pulse) of the laser used for FLIM resulted in requirement of about 20 averages at a pixel to obtain a decent SNR. The pixel rate was 2ms. These limitations were addressed in the second generation OCT-FLIM system. The new FOV of the system was 16x16mm^2, providing comfortable coverage of the entire circumference. Also, we were able to increase the axial scan depth with a swept source laser attributing ~3mm fall-off and 1310nm as the center wavelength. We also significantly improved the SNR of the FLIM emission using a laser with higher pulse energy (1300nJ per pulse). The number of averages required was reduced to 2 and, consequently, the pixel rate has increased ten folds to 200μs. The balance between the increase in the power of the laser and decrease in its dwell-time per pixel provided exposure of the sample within ANSI limit.

The second generation OCT-FLIM system was used to image post-mortem human coronary arteries *ex-vivo*. To date, we have imaged 147 samples from 42 autopsy cases. These samples were 5-12mm in circumference and their length varied between 5-250mm. Samples with length longer than the maximum FOV were imaged in parts, translating the sample longitudinally. The resulting sections of images were then merged to form a mosaic of the entire sample. This library of human arterial OCT-FLIM dataset will be used to train an algorithm for automated atherosclerosis characterization.

In future, the exogenous FLIM system may be used to image non fluorescing molecules like Vascular cell adhesion molecule 1 (VCAM-1) [83] and oxidized low-density lipoprotein (oxLDL) receptor, LOX-1 [13]. These are known to be few of the

responsible molecules for the initiation and progress of atherosclerosis. VCAM-1 plays a role in infiltration of leukocytes into the endothelial cells. LOX-1 binds with oxidized-LDL to generate lipids that initiate and maintain an active inflammatory process in intima [13]. Research suggests that inhibition of these molecules could prevent or reduce atherosclerosis [84]. These molecules have been studied using modalities such as Magnetic Resonance Imaging (MRI), Near Infrared fluorescence imaging and intravascular ultrasound imaging [85-87]. For each of the investigations, VCAM-1 and LOX-1 were conjugated to anti-VCAM-1 and anti-LOX-1, respectively and were tagged with molecules that respond to the modalities. For fluorescence spectroscopy, anti-VCAM1 and anti-LOX-1 can be tagged with an Alexa Fluor or a dye with similar characteristics [88]. We hypothesize that we could use similar method to image them and relate their activity with corresponding morphological and biochemical changes. A more ambitious study could be to investigate them over time to understand the efficacy of their inhibitor or drug [89].

Similarly, another future work entails enhancement of the system for experiments *in vivo*. The sample arm will be replaced with a multimodal fiber-based endoscope with similar or improved lateral resolution and depth of focus, and minimal chromatic aberration. Further, an FPGA can be programmed for real-time processing of the OCT-FLIM data and for easy reconstruction of the image to one that clinicians can appreciate. Moreover, automated characterization of the state of atherosclerosis can provide real-time diagnosis of the disease during surgery or clinical examinations.

7. SUMMARY

Morbidity and mortality due to oral cancer and atherosclerosis may be reduced by being able to diagnose them at all stages. The progressions of these diseases are accompanied by the change in the morphology and biochemistry of the tissue. In order to be able to diagnose them at all stages, detailed information on the tissue is needed. This is possible if both of the biomarkers-morphology and biochemistry- are probed simultaneously.

The property of light-tissue interaction changes with the modification in the morphology and biochemistry of the tissue. Therefore, optical imaging modalities can be used to probe these changes to diagnose oral cancer and atherosclerosis. Unfortunately, an individual modality doesn't have the capability to probe all the biomarkers. Therefore, in recent years, researchers have developed and tested combined multi-modal systems that are able to assess the morphology and the biochemistry. Such imaging tools combine the strengths of different modalities and is superior to any of the constituent modality considered alone.

Two suitable optical imaging modalities for the diagnosis of oral cancer and atherosclerosis are Optical Coherence Tomography (OCT) and Fluorescence Lifetime Imaging Microscopy (FLIM). OCT provides high resolution images of morphology of a tissue up to a depth of 1mm. On the contrary, FLIM furnishes biochemical images based on the emission from fluorophores on the tissue. These fluorophores may be endogenous or exogenous. Endogenous fluorescence is contributed by components such as NADH,

FAD, collagen in oral tissue or collagen LDL and elastin in arterial intima. Exogenous fluorescence is provided by dyes that are used to tag the non-fluorescing molecules of interest.

We have developed combined systems with OCT and FLIM and have validated their ability to image oral tissues and artery. In this dissertation, two such systems were designed, built and validated.

The first OCT-FLIM system was built by incorporating spectral domain OCT, and multi-spectral FLIM with the capability to acquire autofluorescence. The operating wavelengths for OCT and FLIM were 830nm and 355nm. The maximum A-scan rate was 53 kHz and the maximum repetition rate of the laser used for FLIM was 50 kHz. The lateral resolution was 13.33µm and 100µm, respectively. The axial resolution for OCT was 7.6µm. Maximum FOV was 4mmx4mm. This system was used to image hamster cheek pouches with oral cancer and their controls *in vivo*. Additionally, postmortem human coronary arteries were imaged *ex vivo* using the system. The OCT and FLIM images obtained from these experiments were complementary to each other.

The second OCT-FLIM system combined swept source OCT with multi-spectral FLIM, which allowed simultaneous endogenous and exogenous emission acquisition. This system possessed better penetration depth and SNR. The operating wavelength of the swept source laser was 1310nm and its one directional sweep-rate was 50 kHz. FLIM utilized lasers with wavelengths 355nm and 532nm to excite endogenous and exogenous fluorophores, respectively. Both were pulsed at 10 kHz and interleaved such that the signal due to these excitations could be acquired alternately. This supported acquisition

of the endogenous and exogenous emissions simultaneously using a single detector. The lateral resolution was 34μm and 120μm, respectively. The maximum FOV was 16mmx16mm. This system was tested on Watanabe rabbit aorta with and without conjugation of Alexa Fluor 532. The results provided the images of the morphology, endogenous fluorescence and exogenous fluorescence of the aorta, validating the performance of the system. This OCT-FLIM system was used to image postmortem human coronary arteries *ex vivo*.

Future work for this project involves replacement of the sample arm of the system with an endoscope, and study of some specific tagged molecules that play an important role in atherosclerosis.

REFERENCES

[1] J. Park, J. A. Jo, S. Shrestha, P. Pande, Q. Wan, and B. E. Applegate, "A dual-modality optical coherence tomography and fluorescence lifetime imaging microscopy system for simultaneous morphological and biochemical tissue characterization," *Biomed Opt Express,* vol. 1, pp. 186-200, 2010.

[2] T. O. C. Foundation. (2015). *Oral Cancer Facts*. Available: http://www.oralcancerfoundation.org/facts/

[3] O. C. Foundation. (2011, Feb 16). *Oral Cancer Facts*. Available: http://oralcancerfoundation.org/facts/index.htm

[4] W. H. Organization. (2014). *The top 10 causes of death*. Available: http://www.who.int/mediacentre/factsheets/fs310/en/

[5] B. Zarzycka, G. A. Nicolaes, and E. Lutgens, "Targeting the adaptive immune system: new strategies in the treatment of atherosclerosis," *Expert Rev Clin Pharmacol,* vol. 8, pp. 297-313, May 2015.

[6] I. F. Charo and R. Taub, "Anti-inflammatory therapeutics for the treatment of atherosclerosis," *Nat Rev Drug Discov,* vol. 10, pp. 365-76, May 2011.

[7] E. S. Matheny, N. M. Hanna, W. G. Jung, Z. Chen, P. Wilder-Smith, R. Mina-Araghi, and M. Brenner, "Optical coherence tomography of malignancy in hamster cheek pouches," *Journal of Biomedical Optics,* vol. 9, pp. 978-81, Sep-Oct 2004.

[8] P. Wilder-Smith, W. G. Jung, M. Brenner, K. Osann, H. Beydoun, D. Messadi, and Z. Chen, "In vivo optical coherence tomography for the diagnosis of oral malignancy," *Lasers Surg Med,* vol. 35, pp. 269-75, 2004.

[9] P. Wilder-Smith, K. Lee, S. Guo, J. Zhang, K. Osann, Z. Chen, and D. Messadi, "In vivo diagnosis of oral dysplasia and malignancy using optical coherence tomography: preliminary studies in 50 patients," *Lasers Surg Med,* vol. 41, pp. 353-7, Jul 2009.

[10] P. Wilder-Smith, T. Krasieva, W. G. Jung, J. Zhang, Z. Chen, K. Osann, and B. Tromberg, "Noninvasive imaging of oral premalignancy and malignancy," *Journal of Biomedical Optics,* vol. 10, p. 051601, Sep-Oct 2005.

[11] P. Wilder-Smith, K. Osann, N. Hanna, N. El Abbadi, M. Brenner, D. Messadi, and T. Krasieva, "In vivo multiphoton fluorescence imaging: a novel approach to oral malignancy," *Lasers Surg Med,* vol. 35, pp. 96-103, 2004.

[12] I. Georgakoudi, B. C. Jacobson, M. G. Muller, E. E. Sheets, K. Badizadegan, D. L. Carr-Locke, C. P. Crum, C. W. Boone, R. R. Dasari, J. Van Dam, and M. S. Feld, "NAD(P)H and collagen as in vivo quantitative fluorescent biomarkers of epithelial precancerous changes," *Cancer Res,* vol. 62, pp. 682-687, Feb 1 2002.

[13] D. J. Rader and A. Daugherty, "Translating molecular discoveries into new therapies for atherosclerosis," *Nature,* vol. 451, pp. 904-13, Feb 21 2008.

[14] M. H. Niemz, *laser-Tissue Interactions- Fundamentals and Applications*, 3 ed.: Springer-Verlag Berlin Heidelberg, 2004.

[15] Z. G. Wang, D. B. Durand, M. Schoenberg, and Y. T. Pan, "Fluorescence guided optical coherence tomography for the diagnosis of early bladder cancer in a rat model," *J Urol,* vol. 174, pp. 2376-81, Dec 2005.

[16] T. J. Römer, J. F. Brennan, G. J. Puppels, A. H. Zwinderman, S. G. van Duinen, A. van der Laarse, A. F. van der Steen, N. A. Bom, and A. V. Bruschke, "Intravascular ultrasound combined with Raman spectroscopy to localize and quantify cholesterol and calcium salts in atherosclerotic coronary arteries," *Arteriosclerosis, thrombosis, and vascular biology,* vol. 20, pp. 478-483, 2000.

[17] Y. Sun, J. Park, D. N. Stephens, J. A. Jo, L. Sun, J. M. Cannata, R. M. Saroufeem, K. K. Shung, and L. Marcu, "Development of a dual-modal tissue diagnostic system combining time-resolved fluorescence spectroscopy and ultrasonic backscatter microscopy," *Rev Sci Instrum,* vol. 80, p. 065104, Jun 2009.

[18] C. A. Patil, N. Bosschaart, M. D. Keller, T. G. van Leeuwen, and A. Mahadevan-Jansen, "Combined Raman spectroscopy and optical coherence tomography device for tissue characterization," *Optics Letters,* vol. 33, pp. 1135-1137, May 15 2008.

[19] H. Fatakdawala, S. Poti, F. Zhou, Y. Sun, J. Bec, J. Liu, D. R. Yankelevich, S. P. Tinling, R. F. Gandour-Edwards, D. G. Farwell, and L. Marcu, "Multimodal in vivo imaging of oral cancer using fluorescence lifetime, photoacoustic and ultrasound techniques," *Biomed Opt Express,* vol. 4, pp. 1724-41, 2013.

[20] H. Makhlouf, K. Perronet, G. Dupuis, S. Leveque-Fort, and A. Dubois, "Simultaneous optically sectioned fluorescence and optical coherence microscopy with full-field illumination," *Opt Lett,* vol. 37, pp. 1613-5, May 15 2012.

[21] C. Vinegoni, T. Ralston, W. Tan, W. Luo, D. L. Marks, and S. A. Boppart, "Integrated structural and functional optical imaging combining spectral-domain optical coherence and multiphoton microscopy," *Applied Physics Letters,* vol. 88, p. 053901, Jan 30 2006.

[22] J. K. Barton, F. Guzman, and A. Tumlinson, "Dual modality instrument for simultaneous optical coherence tomography imaging and fluorescence spectroscopy," *J Biomed Opt,* vol. 9, pp. 618-23, May-Jun 2004.

[23] L. P. Hariri, A. R. Tumlinson, D. G. Besselsen, U. Utzinger, E. W. Gerner, and J. K. Barton, "Endoscopic optical coherence tomography and laser-induced

fluorescence spectroscopy in a murine colon cancer model," *Lasers Surg Med,* vol. 38, pp. 305-13, Apr 2006.

[24] A. R. Tumlinson, L. P. Hariri, U. Utzinger, and J. K. Barton, "Miniature endoscope for simultaneous optical coherence tomography and laser-induced fluorescence measurement," *Appl Opt,* vol. 43, pp. 113-21, Jan 1 2004.

[25] H. Pahlevaninezhad, I. Cecic, A. M. Lee, A. H. Kyle, S. Lam, C. MacAulay, and P. M. Lane, "Multimodal tissue imaging: using coregistered optical tomography data to estimate tissue autofluorescence intensity change due to scattering and absorption by neoplastic epithelial cells," *Journal of Biomedical Optics,* vol. 18, p. 106007, Oct 2013.

[26] H. Pahlevaninezhad, A. M. Lee, S. Lam, C. MacAulay, and P. M. Lane, "Coregistered autofluorescence-optical coherence tomography imaging of human lung sections," *Journal of Biomedical Optics,* vol. 19, p. 36022, Mar 2014.

[27] S. Yuan, C. A. Roney, J. Wierwille, C. W. Chen, B. Xu, G. Griffiths, J. Jiang, H. Ma, A. Cable, R. M. Summers, and Y. Chen, "Co-registered optical coherence tomography and fluorescence molecular imaging for simultaneous morphological and molecular imaging," *Phys Med Biol,* vol. 55, pp. 191-206, Jan 7 2010.

[28] S. Liang, A. Saidi, J. Jing, G. Liu, J. Li, J. Zhang, C. Sun, J. Narula, and Z. Chen, "Intravascular atherosclerotic imaging with combined fluorescence and optical coherence tomography probe based on a double-clad fiber combiner," *Journal of Biomedical Optics,* vol. 17, p. 070501, Jul 2012.

[29] K. Konig, M. Speicher, R. Buckle, J. Reckfort, G. McKenzie, J. Welzel, M. J. Koehler, P. Elsner, and M. Kaatz, "Clinical optical coherence tomography combined with multiphoton tomography of patients with skin diseases," *Journal of Biophotonics,* vol. 2, pp. 389-397, Jul 2009.

[30] P. J. Caspers, G. W. Lucassen, and G. J. Puppels, "Combined in vivo confocal Raman spectroscopy and confocal microscopy of human skin," *Biophysical Journal,* vol. 85, pp. 572-580, Jul 2003.

[31] J. M. Jabbour, S. Cheng, B. H. Malik, R. Cuenca, J. A. Jo, J. Wright, Y. S. Cheng, and K. C. Maitland, "Fluorescence lifetime imaging and reflectance confocal microscopy for multiscale imaging of oral precancer," *Journal of Biomedical Optics,* vol. 18, p. 046012, Apr 2013.

[32] S. Garg, P. W. Serruys, M. van der Ent, C. Schultz, F. Mastik, G. van Soest, A. van der Steen, M. A. Wilder, J. E. Muller, and E. Regar, "First use in patients of a combined near infra-red spectroscopy and intra-vascular ultrasound catheter to identify composition and structure of coronary plaque," *EuroIntervention: journal of EuroPCR in collaboration with the Working Group on Interventional Cardiology of the European Society of Cardiology,* vol. 5, p. 755, 2010.

[33] C. J. Schultz, P. W. Serruys, M. van der Ent, J. Ligthart, F. Mastik, S. Garg, J. E. Muller, M. A. Wilder, A. F. van de Steen, and E. Regar, "First-in-man clinical use of combined near-infrared spectroscopy and intravascular ultrasound: a potential key to predict distal embolization and no-reflow?," *J Am Coll Cardiol,* vol. 56, p. 314, 2010.

[34] T. Kume, T. Akasaka, T. Kawamoto, N. Watanabe, E. Toyota, Y. Neishi, R. Sukmawan, Y. Sadahira, and K. Yoshida, "Assessment of coronary intima--media thickness by optical coherence tomography: comparison with intravascular ultrasound," *Circ J,* vol. 69, pp. 903-7, Aug 2005.

[35] V. K. Ramanujan, J. H. Zhang, E. Biener, and B. Herman, "Multiphoton fluorescence lifetime contrast in deep tissue imaging: prospects in redox imaging and disease diagnosis," *Journal of Biomedical Optics,* vol. 10, p. 051407, Sep-Oct 2005.

[36] M. C. Skala, K. M. Riching, D. K. Bird, A. Gendron-Fitzpatrick, J. Eickhoff, K. W. Eliceiri, P. J. Keely, and N. Ramanujam, "In vivo multiphoton fluorescence lifetime imaging of protein-bound and free nicotinamide adenine dinucleotide in normal and precancerous epithelia," *Journal of Biomedical Optics,* vol. 12, p. 024014, Mar-Apr 2007.

[37] M. C. Skala, J. M. Squirrell, K. M. Vrotsos, J. C. Eickhoff, A. Gendron-Fitzpatrick, K. W. Eliceiri, and N. Ramanujam, "Multiphoton microscopy of endogenous fluorescence differentiates normal, precancerous, and cancerous squamous epithelial tissues," *Cancer Res,* vol. 65, pp. 1180-6, Feb 15 2005.

[38] D. Li, A. Patel, A. Klibanov, C. K. Kramer, G. A. Beller, D. K. Glover, and C. H. Meyer, "Molecular Imaging of Atherosclerotic Plaques Targeted on Oxidized LDL Receptor LOX-1 Using SPECT/CT and Magnetic Resonance.," *Journal of Nuclear Medicine,* vol. 50, pp. 657-658, Apr 1 2009.

[39] D. Li, A. R. Patel, A. Klibanov, C. H. Meyer, M. Ruiz, C. M. Kramer, G. A. Beller, and D. K. Glover, "Detection and assessment of atherosclerotic plaques using a radiolabeled molecular imaging probe targeted to the oxidized low density lipoprotein receptor LOX-1," *European Heart Journal Supplements,* vol. 11, pp. S69-S69, May 2009.

[40] D. Li, A. R. Patel, A. L. Klibanov, C. M. Kramer, M. Ruiz, B. Y. Kang, J. L. Mehta, G. A. Beller, D. K. Glover, and C. H. Meyer, "Molecular Imaging of Atherosclerotic Plaques Targeted to Oxidized LDL Receptor LOX-1 by SPECT/CT and Magnetic Resonance," *Circulation-Cardiovascular Imaging,* vol. 3, pp. 464-472, Jul 2010.

[41] C. K. Lee, M. T. Tsai, H. C. Lee, H. M. Chen, C. P. Chiang, Y. M. Wang, and C. C. Yang, "Diagnosis of oral submucous fibrosis with optical coherence tomography," *Journal of Biomedical Optics,* vol. 14, p. 054008, Sep-Oct 2009.

[42] I. K. Jang, G. J. Tearney, B. MacNeill, M. Takano, F. Moselewski, N. Iftima, M. Shishkov, S. Houser, H. T. Aretz, E. F. Halpern, and B. E. Bouma, "In vivo characterization of coronary atherosclerotic plaque by use of optical coherence tomography," *Circulation,* vol. 111, pp. 1551-1555, Mar 29 2005.

[43] L. Liu, J. A. Gardecki, S. K. Nadkarni, J. D. Toussaint, Y. Yagi, B. E. Bouma, and G. J. Tearney, "Imaging the subcellular structure of human coronary atherosclerosis using micro-optical coherence tomography," *Nat Med,* vol. 17, pp. 1010-4, Aug 2011.

[44] G. J. Tearney, H. Yabushita, S. L. Houser, H. T. Aretz, I. K. Jang, K. H. Schlendorf, C. R. Kauffman, M. Shishkov, E. F. Halpern, and B. E. Bouma, "Quantification of macrophage content in atherosclerotic plaques by optical coherence tomography," *Circulation,* vol. 107, pp. 113-9, Jan 7 2003.

[45] T. Kume, T. Akasaka, T. Kawamoto, Y. Ogasawara, N. Watanabe, E. Toyota, Y. Neishi, R. Sukmawan, Y. Sadahira, and K. Yoshida, "Assessment of coronary arterial thrombus by optical coherence tomography," *American Journal of Cardiology,* vol. 97, pp. 1713-7, Jun 15 2006.

[46] T. Kume, T. Akasaka, T. Kawamoto, N. Watanabe, E. Toyota, Y. Neishi, R. Sukmawan, Y. Sadahira, and K. Yoshida, "Assessment of coronary arterial plaque by optical coherence tomography," *American Journal of Cardiology,* vol. 97, pp. 1172-1175, Apr 15 2006.

[47] I. K. Jang, B. E. Bouma, D. H. Kang, S. J. Park, S. W. Park, K. B. Seung, K. B. Choi, M. Shishkov, K. Schlendorf, E. Pomerantsev, S. L. Houser, H. T. Aretz, and G. J. Tearney, "Visualization of coronary atherosclerotic plaques in patients using optical coherence tomography: comparison with intravascular ultrasound," *J Am Coll Cardiol,* vol. 39, pp. 604-9, Feb 20 2002.

[48] Y. Sun, J. Phipps, D. S. Elson, H. Stoy, S. Tinling, J. Meier, B. Poirier, F. S. Chuang, D. G. Farwell, and L. Marcu, "Fluorescence lifetime imaging microscopy: in vivo application to diagnosis of oral carcinoma," *Opt Lett,* vol. 34, pp. 2081-3, Jul 1 2009.

[49] Y. Sun, J. E. Phipps, J. Meier, N. Hatami, B. Poirier, D. S. Elson, D. G. Farwell, and L. Marcu, "Endoscopic fluorescence lifetime imaging for in vivo intraoperative diagnosis of oral carcinoma," *Microsc Microanal,* vol. 19, pp. 791-8, Aug 2013.

[50] S. Cheng, R. M. Cuenca, B. Liu, B. H. Malik, J. M. Jabbour, K. C. Maitland, J. Wright, Y. S. Cheng, and J. A. Jo, "Handheld multispectral fluorescence lifetime imaging system for in vivo applications," *Biomed Opt Express,* vol. 5, pp. 921-31, Mar 1 2014.

[51] J. Phipps, Y. H. Sun, N. Hatami, M. C. Fishbein, A. Rajaram, R. Saroufeem, and L. Marcu, "Endoscopic Fluorescence Lifetime Imaging Microscopy (FLIM)

Images of Aortic Plaque: An Automated Classification Method," *Photonic Therapeutics and Diagnostics Vi,* vol. 7548, p. 754839, 2010.

[52] J. Phipps, Y. H. Sun, R. Saroufeem, N. Hatami, M. C. Fishbein, and L. Marcu, "Fluorescence lifetime imaging for the characterization of the biochemical composition of atherosclerotic plaques," *Journal of Biomedical Optics,* vol. 16, p. 096018, Sep 2011.

[53] J. E. Phipps, Y. H. Sun, M. C. Fishbein, and L. Marcu, "A fluorescence lifetime imaging classification method to investigate the collagen to lipid ratio in fibrous caps of atherosclerotic plaque," *Lasers in Surgery and Medicine,* vol. 44, pp. 564-571, Sep 2012.

[54] D. G. MacDonald, "Comparison of epithelial dysplasia in hamster cheek pouch carcinogenesis and human oral mucosa," *J Oral Pathol,* vol. 10, pp. 186-91, Jun 1981.

[55] M. Shiomi and T. Ito, "The Watanabe heritable hyperlipidemic (WHHL) rabbit, its characteristics and history of development: a tribute to the late Dr. Yoshio Watanabe," *Atherosclerosis,* vol. 207, pp. 1-7, Nov 2009.

[56] M. E. Brezinski, *Optical coherence tomography: principles and applications*, First ed.: Academic press, 2006.

[57] W. Drexler and J. G. Fujimoto, *Optical coherence tomography: technology and applications*: Springer Science & Business Media, 2008.

[58] C. M. Eigenwillig, B. R. Biedermann, G. Palte, and R. Huber, "K-space linear Fourier domain mode locked laser and applications for optical coherence tomography," *Optics Express,* vol. 16, pp. 8916-37, Jun 9 2008.

[59] J. Xi, L. Huo, J. Li, and X. Li, "Generic real-time uniform K-space sampling method for high-speed swept-source optical coherence tomography," *Optics Express,* vol. 18, pp. 9511-7, Apr 26 2010.

[60] M. Gora, K. Karnowski, M. Szkulmowski, B. J. Kaluzny, R. Huber, A. Kowalczyk, and M. Wojtkowski, "Ultra high-speed swept source OCT imaging of the anterior segment of human eye at 200 kHz with adjustable imaging range," *Optics Express,* vol. 17, pp. 14880-14894, Aug 17 2009.

[61] B. Potsaid, B. Baumann, D. Huang, S. Barry, A. E. Cable, J. S. Schuman, J. S. Duker, and J. G. Fujimoto, "Ultrahigh speed 1050nm swept source/Fourier domain OCT retinal and anterior segment imaging at 100,000 to 400,000 axial scans per second," *Optics Express,* vol. 18, pp. 20029-48, Sep 13 2010.

[62] M. A. Choma, M. V. Sarunic, C. H. Yang, and J. A. Izatt, "Sensitivity advantage of swept source and Fourier domain optical coherence tomography," *Optics Express,* vol. 11, pp. 2183-2189, Sep 8 2003.

[63] J. R. Lakowicz, *Principles of fluorescence spectroscopy*, Third ed.: Springer Science & Business Media, 2006.

[64] M. C. T. B.E.A. Saleh, *Fundamentals of Photonics*, Second ed. New Jersey: John Wiley & Sons. Inc., 2007.

[65] I. Life Technologies. (2015). *Fluorescence spectraviewer*. Available: http://www.lifetechnologies.com/us/en/home/life-science/cell-analysis/labeling-chemistry/fluorescence-spectraviewer.html

[66] J. A. Jo, Q. Y. Fang, T. Papaioannou, and L. Marcu, "Fast model-free deconvolution of fluorescence decay for analysis of biological systems," *Journal of Biomedical Optics*, vol. 9, pp. 743-752, Jul-Aug 2004.

[67] A. S. Dabir, C. A. Trivedi, Y. Ryu, P. Pande, and J. A. Jo, "Fully automated deconvolution method for on-line analysis of time-resolved fluorescence spectroscopy data based on an iterative Laguerre expansion technique," *Journal of Biomedical Optics*, vol. 14, p. 024030, Mar-Apr 2009.

[68] P. Pande and J. A. Jo, "Automated analysis of fluorescence lifetime imaging microscopy (FLIM) data based on the Laguerre deconvolution method," *IEEE Trans Biomed Eng*, vol. 58, pp. 172-81, Jan 2011.

[69] P. Pande, C. A. Trivedi, and J. A. Jo, "Analysis of Fluorescence Lifetime Imaging Microscopy (FLIM) data. Based on a fully automated Laguerre deconvolution method," *Methods Inf Med*, vol. 49, pp. 531-6, 2010.

[70] S. Shrestha, B. E. Applegate, J. Park, X. Xiao, P. Pande, and J. A. Jo, "High-speed multispectral fluorescence lifetime imaging implementation for in vivo applications," *Opt Lett*, vol. 35, pp. 2558-60, Aug 1 2010.

[71] Q. Y. Fang, T. Papaioannou, J. A. Jo, R. Vaitha, K. Shastry, and L. Marcu, "Time-domain laser-induced fluorescence spectroscopy apparatus for clinical diagnostics," *Review of Scientific Instruments*, vol. 75, pp. 151-162, Jan 2004.

[72] S. T. Flock, S. L. Jacques, B. C. Wilson, W. M. Star, and M. J. C. Vangemert, "Optical-Properties of Intralipid - a Phantom Medium for Light-Propagation Studies," *Lasers in Surgery and Medicine*, vol. 12, pp. 510-519, 1992.

[73] J. L. Brandon, C. J. Conti, L. S. Goldstein, J. DiGiovanni, and I. B. Gimenez-Conti, "Carcinogenic effects of MGP-7 and B[a]P on the hamster cheek pouch," *Toxicol Pathol*, vol. 37, pp. 733-40, Oct 2009.

[74] N. G. Ghoshal and H. S. Bal, "Histomorphology of the hamster cheek pouch," *Lab Anim*, vol. 24, pp. 228-33, Jul 1990.

[75] D. G. Farwell, J. D. Meier, J. Park, Y. Sun, H. Coffman, B. Poirier, J. Phipps, S. Tinling, D. J. Enepekides, and L. Marcu, "Time-Resolved Fluorescence Spectroscopy as a Diagnostic Technique of Oral Carcinoma Validation in the Hamster Buccal Pouch Model," *Archives of Otolaryngology-Head & Neck Surgery*, vol. 136, pp. 126-133, Feb 2010.

[76] P. Thomas, P. Pande, F. Clubb, J. Adame, and J. A. Jo, "Biochemical Imaging of Human Atherosclerotic Plaques with Fluorescence Lifetime Angioscopy," *Photochemistry and Photobiology,* vol. 86, pp. 727-731, May-Jun 2010.

[77] K. Arakawa, K. Isoda, T. Ito, K. Nakajima, T. Shibuya, and F. Ohsuzu, "Fluorescence analysis of biochemical constituents identifies atherosclerotic plaque with a thin fibrous cap," *Arterioscler Thromb Vasc Biol,* vol. 22, pp. 1002-7, Jun 1 2002.

[78] L. Marcu, J. A. Jo, Q. Fang, T. Papaioannou, T. Reil, J. H. Qiao, J. D. Baker, J. A. Freischlag, and M. C. Fishbein, "Detection of rupture-prone atherosclerotic plaques by time-resolved laser-induced fluorescence spectroscopy," *Atherosclerosis,* vol. 204, pp. 156-64, May 2009.

[79] D. Magde, G. E. Rojas, and P. G. Seybold, "Solvent dependence of the fluorescence lifetimes of xanthene dyes," *Photochemistry and Photobiology,* vol. 70, pp. 737-744, Nov 1999.

[80] P. Pande, S. Shrestha, J. Park, M. J. Serafino, I. Gimenez-Conti, J. Brandon, Y. S. Cheng, B. E. Applegate, and J. A. Jo, "Automated classification of optical coherence tomography images for the diagnosis of oral malignancy in the hamster cheek pouch," *Journal of Biomedical Optics,* vol. 19, p. 086022, Aug 2014.

[81] J. Park, P. Pande, S. Shrestha, F. Clubb, B. E. Applegate, and J. A. Jo, "Biochemical characterization of atherosclerotic plaques by endogenous multispectral fluorescence lifetime imaging microscopy," *Atherosclerosis,* vol. 220, pp. 394-401, Feb 2012.

[82] J. A. Jo, J. Park, P. Pande, S. Shrestha, M. J. Serafino, J. d. J. R. Jimenez, F. Clubb, B. Walton, L. M. Buja, and J. E. Phipps, "Simultaneous morphological and biochemical endogenous optical imaging of atherosclerosis," *European Heart Journal-Cardiovascular Imaging,* p. jev018, 2015.

[83] M. I. Cybulsky, K. Iiyama, H. Li, S. Zhu, M. Chen, M. Iiyama, V. Davis, J. C. Gutierrez-Ramos, P. W. Connelly, and D. S. Milstone, "A major role for VCAM-1, but not ICAM-1, in early atherosclerosis," *J Clin Invest,* vol. 107, pp. 1255-62, May 2001.

[84] J. L. Mehta, N. Sanada, C. P. Hu, J. Chen, A. Dandapat, F. Sugawara, H. Satoh, K. Inoue, Y. Kawase, K. Jishage, H. Suzuki, M. Takeya, L. Schnackenberg, R. Beger, P. L. Hermonat, M. Thomas, and T. Sawamura, "Deletion of LOX-1 reduces atherogenesis in LDLR knockout mice fed high cholesterol diet," *Circ Res,* vol. 100, pp. 1634-42, Jun 8 2007.

[85] F. A. Jaffer, P. Libby, and R. Weissleder, "Molecular and cellular imaging of atherosclerosis: emerging applications," *J Am Coll Cardiol,* vol. 47, pp. 1328-38, Apr 4 2006.

[86] D. Li, A. R. Patel, A. L. Klibanov, C. M. Kramer, M. Ruiz, B. Y. Kang, J. L. Mehta, G. A. Beller, D. K. Glover, and C. H. Meyer, "Molecular imaging of atherosclerotic plaques targeted to oxidized LDL receptor LOX-1 by SPECT/CT and magnetic resonance," *Circ Cardiovasc Imaging*, vol. 3, pp. 464-72, Jul 2010.

[87] A. J. Hamilton, S. L. Huang, D. Warnick, M. Rabbat, B. Kane, A. Nagaraj, M. Klegerman, and D. D. McPherson, "Intravascular ultrasound molecular imaging of atheroma components in vivo," *J Am Coll Cardiol*, vol. 43, pp. 453-60, Feb 4 2004.

[88] J. Klohs, "In vivo Imaging of Vascular Targets Using Near-Infrared fluorescent probes," in *Advanced Fluorescence Reporters in Chemistry and Biology III* vol. 10, A. Demchenko, Ed., ed: Springer, 2011, pp. 313-328.

[89] B. L. Walton, M. Leja, K. C. Vickers, M. Estevez-Fernandez, A. Sanguino, E. Wang, F. J. Clubb, Jr., J. Morrisett, and G. Lopez-Berestein, "Delivery of negatively charged liposomes into the atheromas of Watanabe heritable hyperlipidemic rabbits," *Vasc Med*, vol. 15, pp. 307-13, Aug 2010.